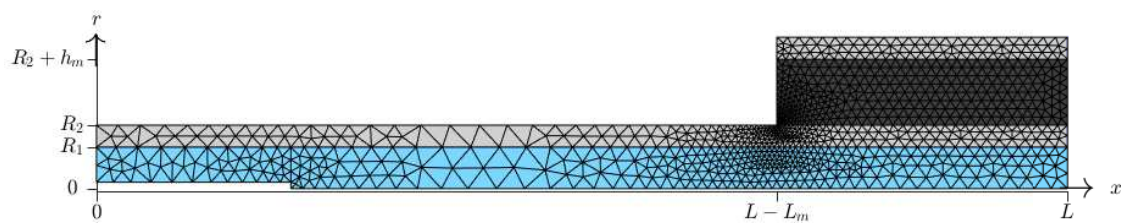Bachelor Thesis

# Theory and numerical modeling of microscale acoustofluidics

William Frisch Møller

s144067

Supervisor: Henrik Bruus

Department of Physics
Technical University of Denmark

19 June 2017

ii

# Abstract

Acoustofluidics is a field of microscale physics that has received increasing interest the past few decades. Specifically interesting is the method of acoustic trapping used for cell separation, which has opened possibilities for faster label-free cancer diagnosis. Thus a thorough understanding of the devices is a necessity. In this thesis we investigate the damping effects of the rubber tubes used to control fluid flow in the acoustic trapping devices by means of numerical simulations.

We start by deriving the governing equations for the first order pressure and displacement fields respectively. We then apply a coordinate transformation to the derived equations, significantly reducing computation times, as it only becomes necessary to model in two rather than three dimensions. Perfectly matched layers are also introduced as the reference point for perfect damping.

Validation of these transformations, then leads to a dedicated investigation of PDMS tubes, using a measure called the standing wave ratio (SWR) to quantify observations. It was found that in general the tubes do have a damping effect on the acoustic fields, however the magnitude of these effects are very volatile to changes in geometry.

In an attempt to maximize damping effects, an investigation of the implementation of a material with linearly varying density was performed. The results seemed to imply that there is a region of densities for which the acoustic waves become much more travelling in nature, which in turn impacts the traps strength and could thus be of interest.

The results presented in this thesis are a step towards a greater understanding of the previously disregarded damping effects that arise in the laboratories.

# Preface

This bachelor thesis, corresponding to 20 ECTS points, is submitted in partial fulfilment of the requirement for the Bachelor of Science in Engineering degree (Physics and Nanotechnology) at the Technical University of Denmark (DTU). The work was carried out from January 2017 till June 2017 at the Department of Physics in the Theoretical Microfluidics Group (TMF), headed by Professor Henrik Bruus.

I firstly want to thank my supervisor Henrik Bruus, not only for the introduction to a very interesting field of physics to which I had no prior knowledge, but also for his dedication, interest and guidance which has made the whole process a great pleasure.

Secondly I would like to thank PhD student Mikkel Ley for the insightful comments and genuine helpfulness with the understanding of difficult concepts.

Finally I thank my family for putting up with me through the hard times, not only with respect to this thesis, but also with respect to the Bachelor in general.

*signature*

William Frisch Møller
Department of Physics
Technical University of Denmark
19 June 2017

# Contents

# List of Figures

# List of Tables

# Chapter 1

# Introduction

Acoustofluidics in general and more specifically microscale acoustofluidic devices have been increasingly considered and used in the fields of biology and clinical diagnostics. Specifically, there has been a lot of research and experimentation regarding cell separation in hopes of developing new label-free methods targeted specifically at isolating circulating tumor cells (CTC) [1]. CTC's are in essence cancer cells that are exist in circulating blood, and have been shown to be found in patients with various types of cancer but rarely in healthy patients, making them a viable indicator of whether or not the patient in question has cancer. The basic idea behind label-free methods is to utilize specific physical properties and characteristics of the cells to separate them, most of which are based on the trapping of cells by exploitation of ultrasonic standing waves in microfluidic devices actuated by piezotransducers [2][3][4][5]. However, to do this, a thorough understanding of the acoustic devices used for acoustic trapping is needed, and thus a lot of theoretical research and numerical simulations has been done for various acoustofluidic devices [2][4][5][6].

## 1.1 Simplification of Numerical Models

Typically the numerical models in question are developed in full three dimensions making any simulations of longer devices very computationally heavy and thus, for very long geometries, completely infeasible. In the article "*Three-Dimensional Numerical Modeling of Acoustic Trapping in Glass Capillaries*" by Mikkel W. H. Ley [6] the longest device length simulated was 10 mm, which when compared to the 50 mm capillary presented in the article "*Continuous flow ultrasonic particle trapping in a glass capillary*" by Ian Gralinski [2] is far from optimal. This forms one of the aims of this thesis, namely to transform the typical governing equations from their full three dimensional form to a simple two dimensional form, by use of axis-symmetry. The hope is that by doing so, a better theoretical understanding of longer geometries can be developed.

## 1.2  Damping Effects

Another aim of the thesis, is to get a better understanding of the effects that the rubber tubing used to transport fluid into and out of the acoustic devices have on the acoustic fields. In figure 1.1 we see the standard experimental set-up for ultrasonic particle trapping, and as evident the rubber tubes cover a large part of the device itself and thus could have a significant impact on the acoustic fields within. The reason this is of such great interest, is that the way the acoustic pressure field $p$ and velocity field $\boldsymbol{v}$ (which is directly related to the pressure) behave has a significant impact on the particle trapping force, namely the acoustic radiation force $\boldsymbol{F}^{rad}$. For mixed travelling and standing waves, the radiation force is given by,



Figure 1.1: A picture of a standard microfluidic device used for particle trapping. The picture is taken from "*Acoustic streaming in the transducer plane in ultrasonic particle manipulation devices*" by Junjun Lei [5].

$$\boldsymbol{F}^{rad} = -\frac{4}{3}\pi a_{pa}^3 \left[ \kappa_{fl} \left\langle (f_0 p)\boldsymbol{\nabla} p \right\rangle - \frac{3}{2}\rho_{fl} \left\langle (f_1 \boldsymbol{v}) \cdot \boldsymbol{\nabla} \boldsymbol{v} \right\rangle \right], \qquad (1.1)$$

where, $a_{pa}$, $\kappa_{fl}$, $\rho_{fl}$, $f_0$ and $f_1$ are the particle radius, the fluid compressibility, the fluid density and the monopole and dipole scattering coefficients respectively [6]. Thus it becomes important for the strength of the trap, whether or not the pressure field $p$ is a standing or travelling wave which to a great extent can depend on the potential damping properties of the rubber tubes. A formal introduction to the above mentioned fields will be presented in chapter 2.

## 1.3  Outline

### Chapter 2: The Governing Equations

Due to the long time spent on getting a thorough understanding of the governing equations for acoustics in both fluids and solids, this chapter represents a somewhat thorough explanation and derivation of the equations that form the basis of further investigations. Specifically, we derived the wave equations for the first order pressure and displacement fields through use of perturbation theory and linear elastic solid theory respectively.

### Chapter 3: Coordinate Transformation

In this chapter we introduce the weak form formulation and walk through the coordinate transformations required to reduce the governing equations from three to two dimensions. An introduction to perfectly matched layers is also included (PML).

## Chapter 4: Numerical Modelling

We introduce the finite element method (FEM) as well as the general system, which will form the starting point for further simulations. On the basis of this system, we validate the coordinate transformed equations as to ensure they yield the same results as the full three dimensional equations. We also run tests to ensure that the PML is correctly applied to the system.

## Chapter 5: Results

In this chapter we investigate the effects tubes of the kind depicted in figure 1.1 have on the acoustic fields of interest. We also extend the investigation to different damping methods in an attempt to replicate optimal damping as represented by PML.

# Chapter 2

# The Governing Equations

## 2.1 Governing equations of fludics

To mathematically describe the motion of fluids, the Eulerian specification of continuum fields will be adopted. In this picture, we observe how the fields at a fixed position $\boldsymbol{r}$ evolve in time $t$. Consequently the position and time are completely independent variables. In general, the field of an arbitrary physical quantity is described as an average of the quantity in question over a fluid particle of volume $\Delta \mathcal{V}(\boldsymbol{r})$ centered at position $\boldsymbol{r}$ at time $t$. Hence we define the density $\rho(\boldsymbol{r}, t)$ and velocity field $\boldsymbol{v}(\boldsymbol{r}, t)$ as

$$\rho(\boldsymbol{r}, t) \equiv \frac{1}{\Delta \mathcal{V}(\boldsymbol{r})} \sum_{i \in \Delta \mathcal{V}(\boldsymbol{r})} m_i \tag{2.1a}$$

$$\boldsymbol{v}(\boldsymbol{r}, t) \equiv \frac{1}{\rho(\boldsymbol{r}, t)\, \Delta \mathcal{V}(\boldsymbol{r})} \sum_{i \in \Delta \mathcal{V}(\boldsymbol{r})} m_i\, \boldsymbol{v}_i, \tag{2.1b}$$

where the index $i$ refers to individual particles enclosed by the volume $\Delta \mathcal{V}(\boldsymbol{r})$ [7]. Having defined the two most fundamental fields of acoustofluidics, we are now ready to derive the governing equations for fluids using the basic concepts of mass and momentum conservation.

### 2.1.1 The continuity equation

The continuity equation can be derived using the principle of mass conservation. We consider a fixed arbitrary region $\Omega$ in the fluid, where the total mass enclosed $M(\Omega, t)$ as a function of time is given by a volume integral of the density field $\rho(\boldsymbol{r}, t)$ over $\Omega$,

$$M(\Omega, t) = \int_\Omega \mathrm{d}\boldsymbol{r}\, \rho(\boldsymbol{r}, t). \tag{2.2}$$

Due to non-relativistic mass conservation, the only way the total mass $M(\Omega, t)$ can vary in time is due to a mass flux through the surface $\partial \Omega$ of the region $\Omega$. To describe the flux,

we introduce the mass current density $\boldsymbol{J}_M(\boldsymbol{r}, t)$ defined as the mass flow per oriented area per time,

$$\boldsymbol{J}_M(\boldsymbol{r}, t) = \rho(\boldsymbol{r}, t)\boldsymbol{v}(\boldsymbol{r}, t), \tag{2.3}$$

where $\boldsymbol{v}(\boldsymbol{r}, t)$ is the advection velocity. Hence we can write an expression for $\partial_t M(\Omega, t)$ as the surface integral over $\partial\Omega$ of the mass current density defined in equation (2.3),

$$
\begin{aligned}
\partial_t M(\Omega, t) &= \oint_{\partial\Omega} \mathrm{d}a \; (-\boldsymbol{n}) \cdot \boldsymbol{J}_M(\boldsymbol{r}, t) = -\oint_{\partial\Omega} \mathrm{d}a \; \boldsymbol{n} \cdot (\rho(\boldsymbol{r}, t)\boldsymbol{v}(\boldsymbol{r}, t)) \\
&= -\int_\Omega \mathrm{d}\boldsymbol{r} \; \boldsymbol{\nabla} \cdot (\rho(\boldsymbol{r}, t)\boldsymbol{v}(\boldsymbol{r}, t)),
\end{aligned}
\tag{2.4}
$$

where the negative sign of the surface normal vector $\boldsymbol{n}$ ensures that positive flux implies an inflow into the region $\Omega$, and where Gauss's theorem was applied to the vector field $\rho(\boldsymbol{r}, t)\boldsymbol{v}(\boldsymbol{r}, t)$ in the final step of equation (2.4). However, an expression for $\partial_t M(\Omega, t)$ can also be obtained by simply differentiating the expression for $M(\Omega, t)$ obtained in equation (2.2),

$$\partial_t M(\Omega, t) = \partial_t \int_\Omega \mathrm{d}\boldsymbol{r} \; \rho(\boldsymbol{r}, t) = \int_\Omega \mathrm{d}\boldsymbol{r} \; \partial_t \rho(\boldsymbol{r}, t). \tag{2.5}$$

Equating equations (2.4) and (2.5) we get the famous continuity equation,

$$\int_\Omega \mathrm{d}\boldsymbol{r} \; \partial_t \rho(\boldsymbol{r}, t) = -\int_\Omega \mathrm{d}\boldsymbol{r} \; \boldsymbol{\nabla} \cdot (\rho(\boldsymbol{r}, t)\boldsymbol{v}(\boldsymbol{r}, t)) \;\Rightarrow\; \partial_t \rho(\boldsymbol{r}, t) = -\boldsymbol{\nabla} \cdot (\rho(\boldsymbol{r}, t)\boldsymbol{v}(\boldsymbol{r}, t)), \tag{2.6}$$

where we have used that the integrands have to be equal since the volume integral is over an arbitrary region $\Omega$.

### 2.1.2   The Navier-Stokes equation

The second governing equation of fludics is the infamous Navier-Stokes equation, which can be derived on the basis of momentum conservation. Again we consider a fixed region $\Omega$ in the fluid and consider the total momentum $\boldsymbol{P}(\Omega, t)$ enclosed,

$$\boldsymbol{P}(\Omega, t) = \int_\Omega \mathrm{d}\boldsymbol{r} \; \rho(\boldsymbol{r}, t)\boldsymbol{v}(\boldsymbol{r}, t). \tag{2.7}$$

Unlike $M(\Omega, t)$, which could only vary due to advection through the surface $\partial\Omega$ of the fixed region, $\boldsymbol{P}(\Omega, t)$ not only varies due to advection but also due to forces given by Newton's second law. These forces can either be body forces that act on the entire region $\Omega$ such as gravitation, or they can be contact forces that act on the surface $\partial\Omega$ such as pressure and viscosity forces. Hence the rate of change in time of the total enclosed momentum $\partial_t \boldsymbol{P}(\Omega, t)$ can be expressed as,

$$\partial_t \boldsymbol{P}(\Omega, t) = \partial_t \boldsymbol{P}(\Omega, t)^{adv.} + \partial_t \boldsymbol{P}(\Omega, t)^{grav.} + \partial_t \boldsymbol{P}(\Omega, t)^{pres.} + \partial_t \boldsymbol{P}(\Omega, t)^{visc.}. \tag{2.8}$$

Starting with the first term of equation (2.8), we define the momentum current density $\boldsymbol{J}_{\boldsymbol{P}}(\boldsymbol{r}, t)$ similar to the mass current density defined in equation (2.3),

$$\boldsymbol{J}_{\boldsymbol{P}}(\boldsymbol{r}, t) = (\rho(\boldsymbol{r}, t)\boldsymbol{v}(\boldsymbol{r}, t))\boldsymbol{v}(\boldsymbol{r}, t). \tag{2.9}$$

The difference being that $\boldsymbol{J_P}(\boldsymbol{r},t)$ is a tensor of rank two rather than a simple vector. Using equation (2.9) we can write an expression for $\partial_t \boldsymbol{P}(\Omega,t)^{adv.}$ as the surface integral of $\boldsymbol{J_P}(\boldsymbol{r},t)$ over $\partial\Omega$,

$$\partial_t \boldsymbol{P}(\Omega,t)^{adv.} = \oint_{\partial\Omega} \mathrm{d}a \, (-\boldsymbol{n}) \cdot \boldsymbol{J_P}(\boldsymbol{r},t) = -\int_\Omega \mathrm{d}\boldsymbol{r} \, \boldsymbol{\nabla} \cdot (\rho(\boldsymbol{r},t)\boldsymbol{v}(\boldsymbol{r},t)\boldsymbol{v}(\boldsymbol{r},t)), \qquad (2.10)$$

where Gauss's theorem has been applied to the second rank tensor field $\rho(\boldsymbol{r},t)\boldsymbol{v}(\boldsymbol{r},t)\boldsymbol{v}(\boldsymbol{r},t)$. An expression for the second term in equation (2.8) can easily be determined as the volume integral of gravitational force density $\boldsymbol{f}^{grav.}(\boldsymbol{r},t)$ over the region $\Omega$,

$$\partial_t \boldsymbol{P}(\Omega,t)^{grav.} = \int_\Omega \mathrm{d}\boldsymbol{r} \, \boldsymbol{f}^{grav.}(\boldsymbol{r},t) = \int_\Omega \mathrm{d}\boldsymbol{r} \, \rho(\boldsymbol{r},t) \, \boldsymbol{g}(\boldsymbol{r},t), \qquad (2.11)$$

where $\boldsymbol{g}(\boldsymbol{r},t)$ is the acceleration of gravity. The change in total momentum due to pressure can be obtained by a surface integral of the force exerted by pressure over $\partial\Omega$,

$$\partial_t \boldsymbol{P}(\Omega,t)^{pres.} = \oint_{\partial\Omega} \mathrm{d}a \, (-\boldsymbol{n}) \cdot (p(\boldsymbol{r},t)\boldsymbol{1}) = -\int_\Omega \mathrm{d}\boldsymbol{r} \, \boldsymbol{\nabla} \cdot (p(\boldsymbol{r},t)\boldsymbol{1}) = -\int_\Omega \mathrm{d}\boldsymbol{r} \, \boldsymbol{\nabla}p(\boldsymbol{r},t)$$
$$(2.12)$$

where $\boldsymbol{1}$ is the identity matrix. The final contribution comes from the viscous friction that occurs at the surface of the fixed region $\partial\Omega$. This interaction can be expressed using the Cauchy stress tensor $\boldsymbol{\sigma}'(\boldsymbol{r},t)$, which is a tensor of rank two where element $\sigma'_{i,j}(\boldsymbol{r},t)$ denotes the $i$th component of the frictional force per unit area acting on a surface with its normal oriented parallel to the unit vector $\hat{\boldsymbol{e}}_j$ (where $i,j = x,y,z$). Hence the change in total momentum due to viscosity must be given by,

$$\partial_t \boldsymbol{P}(\Omega,t)^{visc.} = \oint_{\partial\Omega} \mathrm{d}a \, \boldsymbol{n} \cdot \boldsymbol{\sigma}'(\boldsymbol{r},t) = \int_\Omega \mathrm{d}\boldsymbol{r} \, \boldsymbol{\nabla} \cdot \boldsymbol{\sigma}'(\boldsymbol{r},t). \qquad (2.13)$$

Inserting equations (2.10), (2.11), (2.12) and (2.13) into equation (2.8) and dropping the position and time dependence we get,

$$\partial_t \boldsymbol{P} = \int_\Omega \mathrm{d}\boldsymbol{r} \, -\boldsymbol{\nabla} \cdot (\rho\boldsymbol{v}\boldsymbol{v}) + \rho\boldsymbol{g} - \boldsymbol{\nabla}p + \boldsymbol{\nabla} \cdot \boldsymbol{\sigma}'. \qquad (2.14)$$

However an expression for $\partial_t \boldsymbol{P}$ can also be gotten from differentiating equation (2.7) with respect to time,

$$\partial_t \boldsymbol{P} = \partial_t \int_\Omega \mathrm{d}\boldsymbol{r} \, \rho\boldsymbol{v} = \int_\Omega \mathrm{d}\boldsymbol{r} \, \partial_t(\rho\boldsymbol{v}). \qquad (2.15)$$

Equating equations (2.14) and (2.15) and using the fact that the integrands must be equal given the arbitrariness of $\Omega$, we get the following expression:

$$\partial_t(\rho\boldsymbol{v}) = -\boldsymbol{\nabla} \cdot (\rho\boldsymbol{v}\boldsymbol{v}) + \rho\boldsymbol{g} - \boldsymbol{\nabla}p + \boldsymbol{\nabla} \cdot \boldsymbol{\sigma}' \qquad (2.16)$$

We can now use the continuity equation (2.6) to further simplify the above expression ultimately obtaining the general Navier-Stokes equation,

$$(-\boldsymbol{\nabla} \cdot (\rho\boldsymbol{v}))\boldsymbol{v} + \rho\partial_t\boldsymbol{v} = (-\boldsymbol{\nabla} \cdot (\rho\boldsymbol{v}))\boldsymbol{v} - \rho\boldsymbol{v}(\nabla \cdot \boldsymbol{v}) + \rho\boldsymbol{g} - \boldsymbol{\nabla}p + \boldsymbol{\nabla} \cdot \boldsymbol{\sigma}' \Rightarrow$$
$$\rho\left[\partial_t\boldsymbol{v} + (\boldsymbol{v} \cdot \boldsymbol{\nabla})\boldsymbol{v}\right] = \boldsymbol{\nabla} \cdot \boldsymbol{\sigma}' - \boldsymbol{\nabla}p + \rho\boldsymbol{g}. \qquad (2.17)$$

In order to further elaborate on the Navier-Stokes equation, we will insert an expression for the Cauchy stress tensor. We notice that it is only possible to have a non-zero contribution from the stress tensor if the fluid particles move relative to each other, in other words the stress tensor can only depend on the spatial derivatives of the velocity. Knowing that in general the velocity gradients in acoustofluidics are very small, we can safely assume that only first order derivatives will appear. It thus is no big surprise that the Cauchy stress tensor can be expressed as follows,

$$\boldsymbol{\sigma'} = \eta \left( \boldsymbol{\nabla v} + (\boldsymbol{\nabla v})^T + (\beta - 1)(\boldsymbol{\nabla} \cdot \boldsymbol{v})\mathbf{1} \right), \tag{2.18}$$

where $\eta$ is the dynamic shear viscosity and the term in front of the divergence of the velocity field, $\eta(\beta - 1)$, is the compressibility-induced dilatational viscosity [7]. The term $\beta$ is therefore related to the ratio between the before-mentioned types of viscosity. By insertion of equation (2.18) into equation (2.17) and assuming the fluid is Newtonian such that the viscosity coefficients $\eta$ and $\beta$ are considered constants, we get the celebrated Navier-Stokes equation for Newtonian fluids,

$$\rho \left[ \partial_t \boldsymbol{v} + (\boldsymbol{v} \cdot \boldsymbol{\nabla})\boldsymbol{v} \right] = \boldsymbol{\nabla} \cdot \left[ \eta \left( \boldsymbol{\nabla v} + (\boldsymbol{\nabla v})^T + (\beta - 1)(\boldsymbol{\nabla} \cdot \boldsymbol{v})\mathbf{1} \right) \right] - \boldsymbol{\nabla} p + \rho \boldsymbol{g}$$
$$= -\boldsymbol{\nabla} p + \eta \nabla^2 \boldsymbol{v} + \beta \eta \boldsymbol{\nabla}(\boldsymbol{\nabla} \cdot \boldsymbol{v}) + \rho \boldsymbol{g}. \tag{2.19}$$

### 2.1.3   First Order Perturbation

In the following section we intend to derive the Helmholtz equation for the pressure field in fluids. This will be accomplished using first order perturbation theory together with the Navier-Stokes equation (2.19) and the continuity equation (2.6). Consider a stationary ($\boldsymbol{v}_0 = 0$) liquid with constant density $\rho_0$ and constant pressure $p_0$. We will now introduce the fields of the fluid to a tiny perturbation (denoted with subscript 1) such that the total fields can be expressed as,

$$\rho = \rho_0 + \rho_1 \quad , \quad p = p_0 + p_1 \quad \text{and} \quad \boldsymbol{v} = \boldsymbol{v}_1. \tag{2.20}$$

As to reduce the number of fields in the expressions to come, we will expand the expression for the pressure field such that the perturbation $p_1$ is approximated by the expression $\left( \frac{\partial p}{\partial \rho} \right) \rho_1$. We notice that the derivative has the dimensions of velocity squared, and for reasons that will appear later on in the derivation denote it by $c_0^2$, such that the total pressure field becomes,

$$p = p_0 + c_0^2 \rho_1. \tag{2.21}$$

Inserting equations (2.20) and (2.21) into the continuity equation (2.6) and the Navier-Stokes equation (2.19), where we have absorbed the gravitational term into the pressure term such that the pressure also accounts for the force of gravity, we get,

$$\partial_t(\rho_0 + \rho_1) = -\boldsymbol{\nabla} \cdot ((\rho_0 + \rho_1)\boldsymbol{v}_1) \ \Rightarrow \ \partial_t \rho_1 \approx -\rho_0 \boldsymbol{\nabla} \cdot \boldsymbol{v}_1, \tag{2.22}$$

and,

$$(\rho_0 + \rho_1)\partial_t \boldsymbol{v}_1 = -\boldsymbol{\nabla}(p_0 + c_0^2 \rho_1) - (\rho_0 + \rho_1)(\boldsymbol{v}_1 \cdot \boldsymbol{\nabla})\boldsymbol{v}_1 + \eta \nabla^2 \boldsymbol{v}_1 + \beta \eta \boldsymbol{\nabla}(\boldsymbol{\nabla} \cdot \boldsymbol{v}_1) \ \Rightarrow$$
$$\rho_0 \partial_t \boldsymbol{v}_1 \approx -c_0^2 \boldsymbol{\nabla} \rho_1 + \eta \nabla^2 \boldsymbol{v}_1 + \beta \eta \boldsymbol{\nabla}(\boldsymbol{\nabla} \cdot \boldsymbol{v}_1), \tag{2.23}$$

where we have chosen to neglect all second order terms. Taking the time derivative of equation (2.22) and inserting equation (2.23) in the resulting expression we get,

$$\partial_t^2 \rho_1 = -\boldsymbol{\nabla} \cdot (\rho_0 \partial_t \boldsymbol{v}_1) = c_0^2 \nabla^2 \rho_1 + \eta(1 + \beta)\nabla^2(\boldsymbol{\nabla} \cdot \boldsymbol{v}_1). \tag{2.24}$$

Using equation (2.22) to express the divergence of the velocity field in terms of the density field we get,

$$\partial_t^2 \rho_1 = \left( c_0^2 + \frac{\eta(1 + \beta)}{\rho_0} \partial_t \right) \nabla^2 \rho_1. \tag{2.25}$$

In order to get rid of the partial time derivative, we will assume that all first order fields have a harmonic time dependence,

$$\rho_1(\boldsymbol{r}, t) = \rho_1(\boldsymbol{r})e^{-i\omega t} \quad , \quad p_1(\boldsymbol{r}, t) = p_1(\boldsymbol{r})e^{-i\omega t} \quad \text{and} \quad \boldsymbol{v}_1(\boldsymbol{r}, t) = \boldsymbol{v}_1(\boldsymbol{r})e^{-i\omega t}, \tag{2.26}$$

where $\omega$ is the angular frequency of the acoustic field. This is not a restrictive condition since it is possible to create any arbitrary time dependence from an infinite superposition of the complex exponentials $e^{-i\omega t}$. In other words, if a solution to the fields with the above time dependencies is found, a solution to any time dependence can be constructed from a simple weighted sum of these solutions with differing angular frequencies. Having implemented the assumption, we quickly realise that the partial time derivative $\partial_t$ in equation (2.25) can be replaced by $i\omega$, hence the equation simplifies to,

$$-\omega^2 \rho_1 = \left( c_0^2 - \frac{i\omega\eta(1 + \beta)}{\rho_0} \right) \nabla^2 \rho_1 \;\Rightarrow\; -\frac{\omega^2}{c_0^2} p_1 = \left( 1 - \frac{i\omega\eta(1 + \beta)}{c_0^2 \rho_0} \right) \nabla^2 p_1, \tag{2.27}$$

where we have used the fact that $p_1 = c_0^2 \rho_1$. Essentially we have now arrived at an expression that describes the pressure field in a fluid subjected to a tiny perturbation. However, because the factor $\frac{\omega\eta(1+\beta)}{c_0^2\rho_0}$ is in the order of $10^{-5}$ for acoustic frequencies in the order of MHz [7], we can Taylor expand the expression as to arrive at a simpler expression. Letting $q = \frac{\omega\eta(1+\beta)}{c_0^2\rho_0} \ll 1$ and introducing the wavenumber $k_0 = \frac{\omega}{c_0}$ we have,

$$\nabla^2 p_1 = -k_0^2 \frac{1}{1 - iq} p_1 = -k_0^2 \frac{1 + iq}{1 + q^2} p_1 \approx -k_0^2(1 + iq)p_1 \approx -k_0^2 \left( 1 + i\frac{q}{2} \right)^2 p_1. \tag{2.28}$$

Letting $\Gamma_f = \frac{q}{2}$ be the viscous damping factor, and by introduction of the complex-valued wavenumber $k_f = (1 + i\Gamma)k_0$ we arrive at the Helmholtz equation for a damped wave with wavenumber $k_f$, angular frequency $\omega$ and propagation velocity $c_0$,

$$\nabla^2 p_1 = -k_0^2(1 + i\Gamma_f)^2 p_1 = -k_f^2 p_1 \quad , \quad \Gamma_f = \frac{\omega\eta(1 + \beta)}{2c_0^2 \rho_0}. \tag{2.29}$$

## 2.2 Governing equations of elastic solids

For the purpose of this thesis, knowing how acoustic pressure waves propagate in fluids does not suffice since in the laboratory, the fluid is enclosed in a solid medium. It is

hence necessary to develop a mathematical theory to describe acoustic waves in solids. This is the aim of the following section. The general theory of elastic solids is based on three basic concepts, the displacement $\boldsymbol{u}$, the strain tensor $\boldsymbol{s}$ and the stress tensor $\boldsymbol{\sigma}$. The displacement of a solid element located at $\boldsymbol{r}_0$ is defined as follows,

$$\boldsymbol{u}(\boldsymbol{r}_0, t) \equiv \boldsymbol{r}(t) - \boldsymbol{r}_0, \tag{2.30}$$

where $\boldsymbol{r}$ refers to the new temporary position of the solid element at time $t$ [8]. In the following derivations we will be using index notation such that $r_i$ refers to the $i$th component of the position vector $\boldsymbol{r}$, where $i = x, y, z$, and drop explicitly writing the position and time dependence. We will now consider the infinitesimal distance $\mathrm{d}r_i$ between two neighbouring solid elements, defined on the basis of equation (2.30),

$$\mathrm{d}r_i = \mathrm{d}r_{0i} + \mathrm{d}u_i \approx \mathrm{d}r_{0i} + (\partial_k u_i)\mathrm{d}r_{0k} = (\delta_{ik} + \partial_k u_i)\mathrm{d}r_{0k}, \tag{2.31}$$

where $\delta_{ik}$ is the Kronecker delta, which takes the value 1 when $i = k$ and 0 when $i \neq k$. We have applied a first-order Taylor expansion in the relative displacement, which is a fair approximation for the small deformations typically encountered in the acoustic vibrations to be considered in this thesis [8].

### 2.2.1   The strain and stress tensor

The strain tensor $\boldsymbol{s}$ (with components $s_{ik}$) naturally appears from the scalar product $\mathrm{d}r_j \mathrm{d}r_j$,

$$\mathrm{d}r_j \mathrm{d}r_j = ((\delta_{ji} + \partial_i u_j)\mathrm{d}r_{0i})\,((\delta_{jk} + \partial_k u_j)\mathrm{d}r_{0k}) = (\delta_{ik} + \partial_k u_i + \partial_i u_k + \partial_i u_j \partial_k u_j)\mathrm{d}r_{0i}\mathrm{d}r_{0k}$$

$$\approx (\delta_{ik} + \partial_k u_i + \partial_i u_k)\mathrm{d}r_{0i}\mathrm{d}r_{0k} = (\delta_{ik} + 2s_{ik})\mathrm{d}r_{0i}\mathrm{d}r_{0k} \quad , \quad s_{ik} = \frac{1}{2}(\partial_k u_i + \partial_i u_k). \tag{2.32}$$

The stress tensor on the other hand has already been introduced to some extent in the form of the Cauchy stress tensor when deriving the governing equations of fluidics. Like with the viscous contribution to the change in the total momentum of the fluid, the total intrinsic forces in a solid element must be given by the divergence of the stress tensor,

$$\boldsymbol{f}^{in} = \boldsymbol{\nabla} \cdot \boldsymbol{\sigma}. \tag{2.33}$$

Knowing this, we can calculate the total mechanical work done by a displacement $\delta\boldsymbol{u}$ inside the solid element in an attempt to link the stress and strain tensors,

$$\int_\Omega \mathrm{d}V\ \delta W = \int_\Omega \mathrm{d}V\ \delta u_i \partial_k \sigma_{ik} = \int_\Omega \mathrm{d}V\ \partial_k(\delta u_i \sigma_{ik}) - \int_\Omega \mathrm{d}V\ \partial_k(\delta u_i)\sigma_{ik}$$

$$= \oint_{\partial\Omega} \mathrm{d}A \delta u_i \sigma_{ik} n_k - \int_\Omega \mathrm{d}V\ \delta(\partial_k u_i)\sigma_{ik} = -\frac{1}{2}\int_\Omega \mathrm{d}V\ \delta(\partial_k u_i + \partial_i u_k)\sigma_{ik}, \tag{2.34}$$

$$= -\int_\Omega \mathrm{d}V\ \sigma_{ik}\delta s_{ik}$$

where $\delta W$ is the mechanical work done by the intrinsic force per unit volume and $\Omega$ is an arbitrary fixed region in the elastic solid with surface $\partial\Omega$. Using the fact that the fixed region $\Omega$ is arbitrary we conclude that $\delta W = -\sigma_{ik}\delta s_{ik}$. We now apply the standard thermodynamic expression for the infinitesimal change in the free energy density of the system $F$ to relate the stress and strain,

$$\mathrm{d}F = -S\mathrm{d}T - \mathrm{d}W = -S\mathrm{d}T + \sigma_{ik}\mathrm{d}s_{ik} \;\Rightarrow\; \sigma_{ik} = \left(\frac{\partial F}{\partial s_{ik}}\right)_T. \tag{2.35}$$

Knowing that, at thermal equilibrium, both the strain and stress have to be zero, we can use equation (2.35) to conclude that the free energy density must be written in a quadratic form of the strain,

$$F = F_0 + \frac{1}{2}C_{iklm}s_{ik}s_{lm}, \tag{2.36}$$

where $C_{iklm}$ are the elements of the so called elastic modulus tensor, a tensor of rank four. Fortunately we choose to only consider isotropic solids, meaning that we can have no directional dependence. In other words, we apply the fact that the trace of a tensor is directionally independent to deduce that the only two quadratic terms that can exist in the elastic modulus tensor must be,

$$[\mathrm{Tr}(\boldsymbol{s})]^2 = (s_{jj})^2 = (\boldsymbol{\nabla}\cdot\boldsymbol{u})^2 \quad\text{and}\quad \mathrm{Tr}(\boldsymbol{s}\cdot\boldsymbol{s}) = s_{ik}s_{ik}, \tag{2.37}$$

where the last equality in the first term comes from equation (2.39). Hence the free energy for an isotropic solid becomes,

$$F = F_0 + \frac{1}{2}\lambda s_{jj}^2 + \mu s_{ik}s_{ik}, \tag{2.38}$$

where we have introduced the Lamé coefficients $\lambda$ and $\mu$. We can now find an explicit expression for the stress tensor in terms of the displacement through a combination of equations (2.35), (2.38) and (2.39),

$$\sigma_{ik} = \lambda s_{jj}\delta_{ik} + 2\mu s_{ik} = \lambda(\partial_j u_j)\delta_{ik} + \mu(\partial_i u_k + \partial_k u_i). \tag{2.39}$$

### 2.2.2 Equation of motion

Knowing that the total intrinsic force of a solid is given by the volume integral of $\boldsymbol{\nabla}\cdot\boldsymbol{\sigma}$, we can use Newton's Second Law to derive how the displacement field in an isotropic solid with density $\rho_s$ develops over time,

$$\rho_s\partial_t^2 u_i = f_i^{int.} + f_i^{body} = \partial_k\sigma_{ik} + f_i^{body} = \partial_k(\lambda(\partial_j u_j)\delta_{ik} + \mu(\partial_i u_k + \partial_k u_i)) + f_i^{body}$$
$$= \lambda\partial_i(\partial_j u_j) + \mu\partial_k(\partial_i u_k + \partial_k u_i) + f_i^{body} = \mu\partial_k^2 u_i + (\mu + \lambda)(\partial_i(\partial_k u_k)) + f_i^{body} \;\Rightarrow\;$$
$$\rho_s\partial_t^2 \boldsymbol{u} = \mu\nabla^2\boldsymbol{u} + (\mu + \lambda)\boldsymbol{\nabla}(\boldsymbol{\nabla}\cdot\boldsymbol{u}) + \boldsymbol{f}^{body}.$$
$$\tag{2.40}$$

We now implement the mathematical trick known as the Helmholtz decomposition, where we split the displacement into a transverse divergence-free field $\boldsymbol{u}_T$ and a longitudinal curl-free field $\boldsymbol{u}_L$,

$$\boldsymbol{u} = \boldsymbol{u}_T + \boldsymbol{u}_L \quad , \quad \boldsymbol{\nabla} \cdot \boldsymbol{u}_T = 0 \quad \text{and} \quad \boldsymbol{\nabla} \times \boldsymbol{u}_L = \boldsymbol{0}. \tag{2.41}$$

Inserting the decomposed displacement field into equation (2.40), where we assume no external forces ($\boldsymbol{f}^{body} = \boldsymbol{0}$) we get,

$$\partial_t \boldsymbol{u}_T + \partial_t \boldsymbol{u}_L = \frac{\mu}{\rho_s}(\nabla^2 \boldsymbol{u}_T + \nabla^2 \boldsymbol{u}_L) + \frac{\mu + \lambda}{\rho_s}\nabla^2 \boldsymbol{u}_L = \frac{\mu}{\rho_s}\nabla^2 \boldsymbol{u}_T + \frac{2\mu + \lambda}{\rho_s}\nabla^2 \boldsymbol{u}_L, \tag{2.42}$$

where we have used the identity stating that $\boldsymbol{\nabla}(\boldsymbol{\nabla} \cdot (\boldsymbol{u}_T + \boldsymbol{u}_L)) = \nabla^2 \boldsymbol{u}_L + \boldsymbol{\nabla} \times \boldsymbol{\nabla} \times \boldsymbol{u}_L = \nabla^2 \boldsymbol{u}_L$. As evident from equation (2.42), the equation of motion (2.40) reduces to a simple wave equation with wave speed $c_T$ for a divergence-free displacement field ($\boldsymbol{u}_L = 0$). Likewise, for a curl-free displacement ($\boldsymbol{u}_T = 0$) field the equation reduces to a simple wave equation with wave speed $c_L$. The wave speeds can be expressed as follows,

$$c_T^2 = \frac{\mu}{\rho_s} \quad \text{and} \quad c_L^2 = \frac{2\mu + \lambda}{\rho_s}. \tag{2.43}$$

In general however, the displacement field is a combination of transverse and longitudinal components which is primarily due to coupling in the boundary conditions. We now choose to implement the newly discovered constants $c_L$ and $c_T$ in the expression for the stress tensor $\boldsymbol{\sigma}$ from equation (2.39),

$$\boldsymbol{\sigma} = \lambda(\boldsymbol{\nabla} \cdot \boldsymbol{u})\boldsymbol{1} + \mu\left(\boldsymbol{\nabla}\boldsymbol{u} + (\boldsymbol{\nabla}\boldsymbol{u})^T\right) = \rho_s\left[c_T^2\left(\boldsymbol{\nabla}\boldsymbol{u} + (\boldsymbol{\nabla}\boldsymbol{u})^T\right) + (c_L^2 - 2c_T^2)(\boldsymbol{\nabla} \cdot \boldsymbol{u})\boldsymbol{1}\right]. \tag{2.44}$$

In the derivation of the first order fluid fields, we saw the introduction of a damping term denoted the viscous damping factor $\Gamma_f$. In order to simulate true physical elastic solids, we will introduce a damping term of similar nature to $\Gamma_f$ to the equation of motion (2.40). This is done by simply multiplying the right hand side by the factor $(1 - i\Gamma_s)^2$ where $\Gamma_s \ll 1$ is the bulk damping factor. As we did with the first order fields in the fluid domain, we also assume the displacement field $\boldsymbol{u}$ to have harmonic time dependence such that the partial time derivative on the left hand side of equation (2.40) can be replaced with the factor $i\omega$ where $\omega$ is the angular frequency of the acoustic vibration. Implementing this time dependence together with the damping, (2.40) becomes,

$$-\omega^2\boldsymbol{u} = (1 - i\Gamma_s)^2\frac{1}{\rho_s}\boldsymbol{\nabla}\cdot\boldsymbol{\sigma} = c_T^2(1 - i\Gamma_s)^2\nabla^2\boldsymbol{u} + (c_L^2(1 - i\Gamma_s)^2 - c_T^2(1 + i\Gamma_s)^2)\boldsymbol{\nabla}(\boldsymbol{\nabla}\cdot\boldsymbol{u}). \tag{2.45}$$

Hence we have successfully derived the governing equation for isotropic elastic solids with damping, which in its simplest form can be expressed as follows,

$$\boldsymbol{\nabla} \cdot \boldsymbol{\sigma} = -\frac{\omega^2\rho_s}{(1 - i\Gamma_s)^2}\boldsymbol{u} = -k_s^2\boldsymbol{u} \quad , \quad k_s = \frac{\omega\sqrt{\rho_s}}{1 - i\Gamma_s}. \tag{2.46}$$

# Chapter 3

# Coordinate Transformation

## 3.1 Coordinate Transformation of General Equations

In the following section a coordinate transformation will be applied to the governing equations introduced in Chapter 2. The motivation for doing this, as mentioned in the introduction, lies in the fact that the glass capillaries used in experiments have lengths in the order of $50\,\text{mm}$ [2], meaning that numerically solving the three dimensional governing equations becomes very computationally heavy. For the remainder of this thesis we shall only consider glass capillaries of axis-symmetric geometries. Hence it would make sense to transform the equations from Cartesian to cylindrical coordinates since this allows for the assumption that all fields of interest can be written in the form,

$$F(x, r, \phi) = F(x, r)e^{im\phi}, \tag{3.1}$$

where $m \in \mathbb{Z}^+$ denotes the angular mode of the field. The assumption in equation (3.1) allows for the governing equations to be written in a two-dimensional form, thereby significantly decreasing the computation time and allowing for numerical calculations on longer capillaries.

### 3.1.1 Weak form formulation

Before we can begin the coordinate transformations, it is first necessary to introduce the weak form formulation as we will be implementing the finite element method (FEM) for simulations of microscale acoustic chambers later in the thesis using the software called COMSOL Multiphysics [9]. Hence it becomes important to formulate our governing equations in the above described form. In FEM, a region of space $\Omega$ is discretized in a mesh with many mesh elements, each of finite size and spanned by neighbouring mesh element vertices. Hence the higher the number of mesh elements the more continuous the space becomes at the cost of computational time.

 A mesh cell centered at the vertex $n$ is defined as the collection of mesh elements with a vertex at the location $n$. We can now introduce the concept of a test function $\hat{g}_n$ which is a function defined within the boundaries of a mesh cell centered at $n$ (i.e. takes the
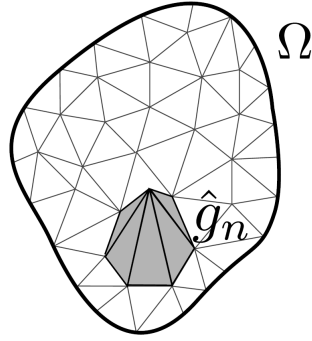
Figure 3.1: A sketch of a mesh of the region enclosed by $\Omega$, with a test function $\hat{g}_n$ centered in the vertex $n$. The sketch is taken from "*Implementation of first- and second-order acoustic perturbation theory in Comsol*" by Henrik Bruus [10].

value 0 everywhere else), that takes the value 1 at $n$ and then continuously decays by a polynomial of order $p$ to 0 at the outer boundaries of the mesh elements defining the mesh cell. In figure 3.1 we see a sample mesh where the test function $\hat{g}_n$ decays linearly (i.e. $p = 1$). The reason for introducing these test functions is due to the fact that neighbouring mesh cells, and thereby test functions, overlap, implying that the set of all test functions make up a non-orthogonal basis. This allows for any function $g(\boldsymbol{r})$ to be approximated by the superposition of $\hat{g}_n$,

$$g(\boldsymbol{r}) \approx \sum_n C_n^g \hat{g}_n(\boldsymbol{r}), \tag{3.2}$$

where $C_n^g$ are the solution coefficients for the function $g(\boldsymbol{r})$, the reason for which will become clear later in the derivation [10]. Having introduced FEM, we can now implement it to the governing equations derived in Chapter 2. As evident from equations (2.29) and (2.46) we are dealing with equations of the following form,

$$\boldsymbol{\nabla} \cdot \boldsymbol{J} - \boldsymbol{F} = 0, \tag{3.3}$$

where $\boldsymbol{J}$ is a generalised flux and $F$ is a generalised force driving that flux. In the case of a scalar equation, like the Helmholtz equation for pressure, the flux is a vector $J_i$ with a scalar divergence and the driving force is a scalar. Explicitly we get the following expressions for equation (2.29),

$$\boldsymbol{J}_f = \boldsymbol{0} \quad \text{and} \quad F_f = \nabla^2 p_1 + k_f^2 p_1. \tag{3.4}$$

One could think that the flux should be $\boldsymbol{\nabla} p_1$, however since the equation is for finding $p_1$ we are looking for a vector current involving $p_1$ and not the gradient $\boldsymbol{\nabla} p_1$ which is directly related to the first order velocity of the fluid $\boldsymbol{v}_1$ ($\boldsymbol{v}_1 = -i\frac{1}{\rho_0 \omega}\boldsymbol{\nabla} p_1$ [7]). For a vector equation, like that of the equation of motion (2.46), the flux is a tensor of rank two $J_{ij}$ with a vector divergence and the driving force is a vector. Explicitly for equation (2.46) we get,

$$\boldsymbol{J}_s = \boldsymbol{\sigma} \quad \text{and} \quad \boldsymbol{F}_s = k_s^2 \boldsymbol{u}. \tag{3.5}$$

By application of the approximation (3.2) to the general form (3.3) for a general field $g(\boldsymbol{r})$, we expect for there to be a defect $d(\boldsymbol{r})$ whose magnitude depends on the granularity of the mesh,

$$\boldsymbol{\nabla} \cdot \boldsymbol{J}\left[g(\boldsymbol{r})\right] - F(\boldsymbol{r}) = d(\boldsymbol{r}). \tag{3.6}$$

Fortunately it so happens that the strong form (3.3) is approximately satisfied if the projection of the defect $d(\boldsymbol{r})$ on every test function $\hat{g}_m(\boldsymbol{r})$ defined in a mesh of volume $\Omega$ is 0,

$$\int_\Omega \mathrm{d}V \; \hat{g}_m(\boldsymbol{r}) \left[\boldsymbol{\nabla} \cdot \boldsymbol{J}\left[g(\boldsymbol{r})\right] - F(\boldsymbol{r})\right] = 0 \; \forall \; m \in \Omega. \tag{3.7}$$

By direct insertion of equation (3.2) into equation (3.7) we have,

$$\int_\Omega \mathrm{d}V \; \hat{g}_m(\boldsymbol{r}) \left[\boldsymbol{\nabla} \cdot \boldsymbol{J}\left[\sum_n C_n^g \hat{g}_n\right] - F(\boldsymbol{r})\right] = 0 \; \Rightarrow$$

$$\sum_n C_n^g \int_\Omega \mathrm{d}V \; \hat{g}_m(\boldsymbol{r}) \boldsymbol{\nabla} \cdot \boldsymbol{J}\left[\hat{g}_n(\boldsymbol{r})\right] - \int_\Omega \mathrm{d}V \; \hat{g}_m(\boldsymbol{r}) F(\boldsymbol{r}) = 0 \; \Rightarrow \; K_{mn} C_n^g = F_m \tag{3.8}$$

where we have assumed that the current operator $J(g(\boldsymbol{r}))$ is linear and introduced the stiffness matrix with elements $K_{mn}$ and the force vector $F_m$, defined below,

$$K_{mn} = \int_\Omega \mathrm{d}V \; \hat{g}_m(\boldsymbol{r}) \boldsymbol{\nabla} \cdot \boldsymbol{J}\left[\hat{g}_n(\boldsymbol{r})\right] \quad, \quad F_m = \int_\Omega \mathrm{d}V \; \hat{g}_m(\boldsymbol{r}) F(\boldsymbol{r}). \tag{3.9}$$

In other words, the weak form formulation becomes a simple matrix inversion problem to find the solution coefficients $C_n^g$, which in turn yields an approximate solution to the equations on strong form.

### 3.1.2 Helmholtz Equation

Having introduced the weak form formulation, we can now return to the coordinate transformation of the governing equations from Cartesian to cylindrical. We start by considering the first order pressure field $p_1(\boldsymbol{r}, t)$, from equation (2.29) we know that the field can be found from the Helmholtz equation,

$$\nabla^2 p_1(\boldsymbol{r}, t) = -k_f^2 p_1(\boldsymbol{r}, t). \tag{3.10}$$

In the following, we will divide through by the harmonic time dependence represented by the complex phase $e^{-i\omega t}$ as to kill the time dependence, simplifying further mathematical treatment. In order transform equation (3.10) from Cartesian coordinates to cylindrical coordinates, the pressure field itself becomes,

$$p_1(\boldsymbol{r}) = p_1(x, y, z) = p_1(x, r, \phi) = p_1(\boldsymbol{r}'), \tag{3.11}$$

where $\boldsymbol{r}'$ denotes the position expressed in cylindrical coordinates. However, the Laplacian does not transform so simply due to the fact that $\partial_\phi \hat{\boldsymbol{e}}_r = \hat{\boldsymbol{e}}_\phi$ and $\partial_\phi \hat{\boldsymbol{e}}_\phi = -\hat{\boldsymbol{e}}_r$. To find

an expression for the Laplacian in cylindrical coordinates we introduce the nabla operator written in cylindrical coordinates,

$$\boldsymbol{\nabla} = \hat{\boldsymbol{e}}_x \partial_x + \hat{\boldsymbol{e}}_r \partial_r + \hat{\boldsymbol{e}}_\phi \frac{1}{r} \partial_\phi. \tag{3.12}$$

The Laplacian thus becomes,

$$\begin{aligned}
\nabla^2 = \boldsymbol{\nabla} \cdot \boldsymbol{\nabla} &= \left( \hat{\boldsymbol{e}}_x \partial_x + \hat{\boldsymbol{e}}_r \partial_r + \hat{\boldsymbol{e}}_\phi \frac{1}{r} \partial_\phi \right) \cdot \left( \hat{\boldsymbol{e}}_x \partial_x + \hat{\boldsymbol{e}}_r \partial_r + \hat{\boldsymbol{e}}_\phi \frac{1}{r} \partial_\phi \right) \\
&= \partial_x^2 + \partial_r^2 + \frac{1}{r} \partial_r + \frac{1}{r^2} \partial_\phi^2 = \partial_x^2 + \frac{1}{r} \partial_r (r \partial_r) + \frac{1}{r^2} \partial_\phi^2.
\end{aligned} \tag{3.13}$$

Inserting equations (3.11) and (3.13) into equation (3.10), we get the cylindrical Helmholtz equation,

$$\partial_x^2 p_1(\boldsymbol{r'}) + \frac{1}{r} \partial_r (r \partial_r p_1(\boldsymbol{r'})) + \frac{1}{r^2} \partial_\phi^2 p_1(\boldsymbol{r'}) = -k_f^2 p_1(\boldsymbol{r'}). \tag{3.14}$$

We now apply the assumption introduced in equation (3.1) in order to reduce the equation to two dimensions. With this, each angle derivative $\partial_\phi$ gives a factor $im$, and thus the equation becomes

$$\partial_x^2 p_1(x, r) + \frac{1}{r} \partial_r (r \partial_r p_1(x, r)) - \frac{m^2}{r^2} p_1(x, r) = -k_f^2 p_1(x, r) \tag{3.15}$$

where we have divided through by the complex phase $e^{im\phi}$ as to remove the angle dependence. We continue by rewriting the equation to the weak form introduced in equation (3.7) using the test function $\tilde{p}_1(x, r)$,

$$\int_{x,r} \tilde{p}_1(x, r) \left[ \partial_x^2 p_1(x, r) + \frac{1}{r} \partial_r (r \partial_r p_1(x, r)) + k_f^2 p_1(x, r) - \frac{m^2}{r^2} p_1(x, r) \right] 2\pi r \mathrm{d}x \mathrm{d}r = 0, \tag{3.16}$$

where the integral has been reduced from a volumetric integral to a two dimensional integral using the fact that the integrand is angle independent. After simplification, we recover the weak form equation of the two dimensional Helmholtz equation,

$$\int_{x,r} \tilde{p}_1(x, r) \left[ \partial_x \left[ 2\pi r \partial_x p_1(x, r) \right] + \partial_r \left[ 2\pi r \partial_r p_1(x, r) \right] + 2\pi p_1(x, r) \left( k_f^2 r - \frac{m^2}{r} \right) \right] \mathrm{d}x \mathrm{d}r = 0, \tag{3.17}$$

where the generalised flux $\boldsymbol{J_p}$ and the the generalised driving force $F_p$ are given as,

$$\boldsymbol{J_p} = 2\pi r \partial_x p_1(x, r) \hat{\boldsymbol{e}}_x + 2\pi r \partial_r p_1(x, r) \hat{\boldsymbol{e}}_r \quad , \quad F_p = 2\pi p_1(x, r) \left( k_f^2 r - \frac{m^2}{r} \right). \tag{3.18}$$

### 3.1.3   Equation of Motion

We will now consider the transformation of the general equation of motion for elastic solids with effective damping introduced in equation (2.46),

$$\boldsymbol{\nabla} \cdot \boldsymbol{\sigma}(\boldsymbol{r}, t) = -k_s^2 \boldsymbol{u}(\boldsymbol{r}, t). \tag{3.19}$$

As with the pressure field we divide through by the complex phase $e^{-i\omega t}$ as to remove the time dependence, and transform the displacement field as follows,

$$\boldsymbol{u}(\boldsymbol{r}) = \boldsymbol{u}(x, y, z) = \boldsymbol{u}(x, r, \phi) = \boldsymbol{u}(\boldsymbol{r'}). \tag{3.20}$$

In order to fully transform the equation, we need to evaluate the dot product $\boldsymbol{\nabla} \cdot \boldsymbol{\sigma}(\boldsymbol{r'})$. In the following we shall drop explicitly writing the position dependence, as to simplify further expressions. Using equation (3.12) we have,

$$\boldsymbol{\nabla} \cdot \boldsymbol{\sigma} = \left( \hat{\boldsymbol{e}}_x \partial_x + \hat{\boldsymbol{e}}_r \partial_r + \hat{\boldsymbol{e}}_\phi \frac{1}{r} \partial_\phi \right) \cdot \boldsymbol{\sigma} = \left( \partial_x \sigma_{xx} + \partial_r \sigma_{rx} + \frac{\sigma_{rx}}{r} + \frac{\partial_\phi \sigma_{\phi x}}{r} \right) \hat{\boldsymbol{e}}_x$$
$$+ \left( \partial_x \sigma_{xr} + \partial_r \sigma_{rr} + \frac{\sigma_{rr}}{r} + \frac{\partial_\phi \sigma_{\phi r}}{r} - \frac{\sigma_{\phi\phi}}{r} \right) \hat{\boldsymbol{e}}_r$$
$$+ \left( \partial_x \sigma_{x\phi} + \partial_r \sigma_{r\phi} + \frac{\sigma_{r\phi}}{r} + \frac{\partial_\phi \sigma_{\phi\phi}}{r} + \frac{\sigma_{\phi r}}{r} \right) \hat{\boldsymbol{e}}_\phi. \tag{3.21}$$

As evident, there are an extra two terms in the $r$ and $\phi$ components of the divergence with opposite signs. These two expressions come from the angle derivatives of the unit vectors $\hat{\boldsymbol{e}}_r$ and $\hat{\boldsymbol{e}}_\phi$. Inserting equation (3.21) into equation (3.19) and using the assumption from equation (3.1), which replaces all angle derivatives $\partial_\phi$ with the factor $im$, and immediately dividing through with the complex phase $e^{im\phi}$ we get the following equation,

$$\boldsymbol{0} = \left( \partial_x \sigma_{xx} + \partial_r \sigma_{rx} + \frac{\sigma_{rx} + im\sigma_{\phi x}}{r} + k_s^2 u_x \right) \hat{\boldsymbol{e}}_x$$
$$+ \left( \partial_x \sigma_{xr} + \partial_r \sigma_{rr} + \frac{\sigma_{rr} - \sigma_{\phi\phi} + im\sigma_{\phi r}}{r} + k_s^2 u_r \right) \hat{\boldsymbol{e}}_r \tag{3.22}$$
$$+ \left( \partial_x \sigma_{x\phi} + \partial_r \sigma_{r\phi} + \frac{\sigma_{r\phi} + \sigma_{\phi r} + im\sigma_{\phi\phi}}{r} + k_s^2 u_\phi \right) \hat{\boldsymbol{e}}_\phi.$$

where all the stress tensor components $\sigma_{ij}(x, r)$ and displacement components $u_k(x, r)$ are functions of the axial and radial coordinates only. Similar to the transformation of the Helmholtz equation, we now rewrite equation (3.22) to the weak form using the test function $\tilde{\boldsymbol{u}}(x, r)$,

$$\int_{x,r} \tilde{\boldsymbol{u}}(x, r) \cdot \begin{bmatrix} \left( \partial_x \sigma_{xx} + \partial_r \sigma_{rx} + \dfrac{\sigma_{rx} + im\sigma_{\phi x}}{r} + k_s^2 u_x \right) \hat{\boldsymbol{e}}_x \\ + \left( \partial_x \sigma_{xr} + \partial_r \sigma_{rr} + \dfrac{\sigma_{rr} - \sigma_{\phi\phi} + im\sigma_{\phi r}}{r} + k_s^2 u_r \right) \hat{\boldsymbol{e}}_r \\ + \left( \partial_x \sigma_{x\phi} + \partial_r \sigma_{r\phi} + \dfrac{\sigma_{r\phi} + \sigma_{\phi r} + im\sigma_{\phi\phi}}{r} + k_s^2 u_\phi \right) \hat{\boldsymbol{e}}_\phi \end{bmatrix} 2\pi r \mathrm{d}x \mathrm{d}r = \boldsymbol{0}.$$

$$\tag{3.23}$$

After simplification we end up with the following expression for the transformed weak form equation of motion in elastic solids,

$$
\int_{x,r} \tilde{\boldsymbol{u}} \cdot \begin{bmatrix} 2\pi k_s^2 r \boldsymbol{u} + (\partial_x [2\pi r\sigma_{xx}] + \partial_r [2\pi r\sigma_{rx}] + 2\pi (\sigma_{rx} + im\sigma_{\phi x})) \, \hat{\boldsymbol{e}}_x \\ + (\partial_x [2\pi r\sigma_{xr}] + \partial_r [2\pi r\sigma_{rr}] + 2\pi (\sigma_{rr} - \sigma_{\phi\phi} + im\sigma_{\phi r})) \, \hat{\boldsymbol{e}}_r \\ + (\partial_x [2\pi r\sigma_{x\phi}] + \partial_r [2\pi r\sigma_{r\phi}] + 2\pi (\sigma_{r\phi} + \sigma_{\phi r} + im\sigma_{\phi\phi})) \, \hat{\boldsymbol{e}}_\phi \end{bmatrix} \mathrm{d}x\mathrm{d}r = \boldsymbol{0}. \quad (3.24)
$$

From equation (3.24) we see that the generalised flux $\boldsymbol{J_u}$ is a 2 by 3 matrix and the generalised driving force $\boldsymbol{F_u}$ is a three dimensional vector,

$$
\boldsymbol{J_u} = 2\pi r \begin{pmatrix} \sigma_{xx} & \sigma_{rx} \\ \sigma_{xr} & \sigma_{rr} \\ \sigma_{x\phi} & \sigma_{r\phi} \end{pmatrix} \quad , \quad \boldsymbol{F_u} = 2\pi \begin{pmatrix} \sigma_{rx} + im\sigma_{\phi x} + k_s^2 r u_x \\ \sigma_{rr} - \sigma_{\phi\phi} + im\sigma_{\phi r} + k_s^2 r u_r \\ \sigma_{r\phi} + \sigma_{\phi r} + im\sigma_{\phi\phi} + k_s^2 r u_\phi \end{pmatrix} \quad (3.25)
$$

## 3.2   Perfectly Matched Layers (PML)

For the purpose of later use, we introduce the concept of a perfectly matched layer (PML). A PML is essentially an artificial absorbing layer for waves used to prevent any reflections thereby simulating open boundary conditions. The reason this is of interest lies in the fact that a PML is the perfect absorber, thereby being a great reference point when attempting to simulate the effects of damping the rubber tubes can have on acoustic chambers. The mathematical implementation of a PML with length $L_{PML}$ is relatively simple. Let us assume we wish to dampen outgoing waves in the $x$ direction, this can be done by a complex-valued coordinate stretching in the $x$ direction within the PML region, which is a region placed in extension to the system in question. This stretching is based on a real-valued function denoted $s(x)$ which takes the value 0 outside the PML region and quadratically increases within the PML region with a smooth transition,

$$
s(x) = k_{PML} \left( \frac{x - L}{L_{PML}} \right)^2 \quad , \quad L \leq x \leq L + L_{PML}, \quad (3.26)
$$

where $L$ is the length along the $x$ axis from the origin to the start of the PML region, and $k_{PML}$ is the absorption strength [6]. In Chapter 4 of the thesis we explore the range of values for $k_{PML}$ that ensure perfect damping, since if the absorption strength is too small then the damping will not be effective thus allowing for possible reflections. On the other hand, if $k_{PML}$ is too large we expect for the wave to be reflected immediately on the boundary of the PML region, due to a too extreme transition, instead of damped. Having defined the function $s(x)$, the mathematical implementation of the coordinate stretching can be expressed as follows,

$$
\partial_x \; \to \; \partial_{\tilde{x}} = \frac{1}{1 + is(x)} \partial_x \quad \text{and} \quad \mathrm{d}x \; \to \; \mathrm{d}\tilde{x} = (1 + is(x))\mathrm{d}x. \quad (3.27)
$$

In other words, $\partial_{\tilde{x}}$ and $\mathrm{d}\tilde{x}$ are to replace the $\partial_x$ and $\mathrm{d}x$ in all equations and boundary conditions of interest.

# Chapter 4

# Numerical Modelling

## 4.1 Discription of system

In the following section we will describe the system we will be modelling using the finite element software COMSOL Multiphysics [9]. Of the many various acoustic chamber designs, we have chosen a system that closely resembles the one presented in "*Continuous flow ultrasonic particle trapping in a glass capillary*" by Ian Gralinski [2]. The main reasons for this lies in the fact that it is of cylindrical geometry, allowing for the application of the coordinate transformations presented in Chapter 3, and the fact that the results found from numerical modelling can to some extent be compared to the experimental findings of the article. According to the article, the glass capillary used for experiments, made of PYREX borosilicate glass had an outer radius of $R_2 = 650 \, \mu$m, an inner radius of $R_1 = 425 \, \mu$m and a total length of $50$ mm, however for the purpose of this thesis we will be modelling a capillary of total length $L_{tot} = 20$ mm (such that $L = 10$ mm) as to reduce the number of resonances in the system as well as to enhance to quality of the simulated results given the limited computational power at hand. The parameters $R_2$, $R_1$ and $L$ are depicted in figure 4.1. As previously mentioned we intend to only model in two
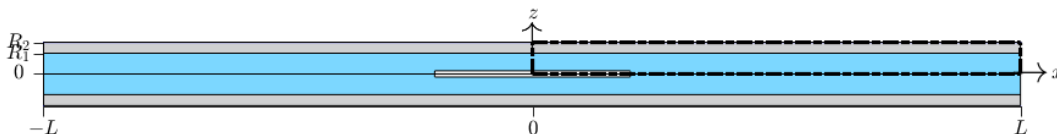


Figure 4.1: Cross-section in the $y = 0$ plane, of the glass capillary which is to form the basis of the investigations to be presented in this thesis. It is based on the capillary described in "*Continuous flow ultrasonic particle trapping in a glass capillary*" by Ian Gralinski [2]. The outer grey rectangles represent the PYREX glass, the cyan blue region represents the water and the grey rectangle in the centre represents the artificial actuator. The dotted rectangle illustrates the two dimensional region which will be modelled.

dimensions using the coordinate transformed governing equations (derived in Chapter 3).

19

The main reason for doing so lies in the fact that by only modelling in two dimensions we are able to significantly reduce computing time, and thereby allow for the simulation of longer geometries that were previously infeasible when modelling in the full three dimensions. Also, by using the lines of symmetry inherent in the geometry we only need to simulate a quarter of the entire cross section, as evident in figure 4.1, which in turn lets us recover a solution of higher resolution. In the experiments the glass capillary was actuated by means of an piezoelectric transducer of approximate dimensions $4 \times 1 \times 0.5 \, \text{mm}^3$ ($L \times W \times H$) that was bonded to the outside of the capillary using a silicon adapter. In other words the actuation was localized on the surface of the capillary. Hence the actuation method is not axis-symmetric meaning that it is not possible to model using our coordinate transformations in two dimensions. A potential workaround would be to simulate an actuating "band" wrapped around the glass chamber with a similar length and height to the transducer. However, it was found in *"Three-Dimensional Numerical Modeling of Acoustic Trapping in Glass Capillaries"* by Mikkel W. H. Ley [6], that an actuation of 0.1 nm at the bottom of a chamber (similar in nature to the actual actuation described in the *"Continuous flow ultrasonic particle trapping in a glass capillary"* by Ian Gralinski [2]) led to displacements of the PYREX glass at the top of the chamber that were an entire order of magnitude greater ($\sim 1 \, \text{nm}$). This significant amplification effect would be neglected with the actuation "band", since such band would constrain the glass to a maximum displacement of the actuation. Hence we have chosen to actuate the chamber by means of a suspended rod in the centre of the fluid domain with the same length as that of the described piezoelectric transducer but with a radius of $R_{act} = \frac{1}{10} R_2$. Although not very realistic, doing this will allow for the glass boundaries to vibrate freely thereby closely resembling the actual method of actuation.

### 4.1.1  Boundary Conditions

Before any computations can be made, it is necessary to define the boundary conditions of the system. As evident in figure 4.1 we have five types boundaries to consider, fluid-air and solid-air, fluid-solid, the boundaries to the symmetry lines and finally the boundaries on the actuator. Starting with the fluid-air and solid-air boundaries, we apply the soft-wall condition for the boundaries between the fluid and air since the surrounding air cannot sustain any appreciable pressure,

$$p_1 = 0. \tag{4.1}$$

For the solid-air boundary we apply the zero-flux condition as we have mass conservation,

$$\boldsymbol{n} \cdot \boldsymbol{\sigma} = \boldsymbol{0}. \tag{4.2}$$

We now consider the fluid-solid boundary. Seen from the fluid at this interface we expect the normal velocity of the solid to be equal to the normal velocity of the liquid [11]. Knowing that that $\boldsymbol{\nabla} p_1 = i\omega\rho_0 \boldsymbol{v}_1$ [7] and due to harmonic time dependence $\boldsymbol{v}_s = -i\omega\boldsymbol{u}$, we get the following boundary condition,

$$\boldsymbol{n} \cdot \boldsymbol{v}_1 = \boldsymbol{n} \cdot \boldsymbol{v}_s \;\Rightarrow\; \frac{-i}{\omega\rho_0}\boldsymbol{n} \cdot \boldsymbol{\nabla} p_1 = -i\omega\boldsymbol{n} \cdot \boldsymbol{u} \;\Rightarrow\; \boldsymbol{n} \cdot \boldsymbol{\nabla} p_1 = \omega^2\rho_0 \boldsymbol{n} \cdot \boldsymbol{u}. \tag{4.3}$$

Seen from the solid we again require a zero-flux, however we now have an extra contribution in the form of the pressure from the liquid, hence

$$\boldsymbol{n} \cdot \boldsymbol{\sigma} + p_1 \boldsymbol{n} = 0 \;\; \Rightarrow \;\; \boldsymbol{n} \cdot \boldsymbol{\sigma} = -p_1 \boldsymbol{n}. \tag{4.4}$$

For the boundaries that lie on the axes of symmetry we must require that there can be no displacement normal to the boundary and that the velocity of the fluid must be zero. This intuitively makes sense, since if the normal components of the displacement and velocity were non-zero at this boundary it would no longer be a line of symmetry. Mathematically we thus have,

$$\boldsymbol{n} \cdot \boldsymbol{u} = 0 \quad \text{and} \quad \frac{-i}{\omega \rho_0} \boldsymbol{n} \cdot \boldsymbol{\nabla} p_1 = 0 \;\; \Rightarrow \;\; \boldsymbol{n} \cdot \boldsymbol{\nabla} p_1 = 0. \tag{4.5}$$

Finally we consider the boundaries between the artificial actuator and the fluid. This boundary is identical to the fluid-solid boundary with the exception that the displacement is simply the maximum actuation amplitude $d_0$ (which will be set to $d_0 = 0.1\,\text{nm}$ for all future simulations) in the radial direction and 0 in the $x$ and $\phi$ directions,

$$\boldsymbol{n} \cdot \boldsymbol{\nabla} p_1 = \omega^2 \rho_0 \boldsymbol{n} \cdot (d_0 \hat{\boldsymbol{e}}_r) \tag{4.6}$$

### 4.1.2 Material parameters

In order to simulate the above described system it is necessary to know the physical parameters of the materials to be modelled. From the axis-symmetric governing equations (3.17) and (3.24), we see that the important fluid parameters happen to be the speed of sound $c_f$ and the viscous damping factor $\Gamma_f$ which is itself a function of the density $\rho_f$, the viscosity parameters $\eta$ and $\beta$, the speed of sound and the angular frequency $\omega$ as evident in equation (2.29). For the solid domain, the parameters of interest are the density $\rho_s$, the bulk damping factor $\Gamma_s$ and the stress tensor $\boldsymbol{\sigma}$ which is a function of the longitudinal and transverse speeds of sound $c_L$ and $c_T$. $c_L$ and $c_T$ can be found from the Young's Modulus $E$ and Poisson's ratio $\nu$ of the solid according to the following expressions [8],

$$c_L^2 = \frac{(1-\nu)}{(1-2\nu)(1+\nu)} \frac{E}{\rho_s} \quad \text{and} \quad c_T^2 = \frac{1}{2(1+\nu)} \frac{E}{\rho_s}. \tag{4.7}$$

In table 4.1 we see the values of the above described parameters. As previously mentioned we will be modelling water in a PYREX glass capillary explaining why these materials are included in table 4.1, polydimethylsiloxane (PDMS) is also included as it will be utilized as the reference material to test for damping phenomena later in the thesis. We see from the table that $\Gamma$ for water is 0.004, however if one calculates using equation (2.29) for $\eta = 0.89\,\text{mPas}$ and $\beta = 3.0$ at $f = 1\,\text{MHz}$ one gets $5 \times 10^{-6}$ a difference of 3 orders of magnitude. The reason for this inconsistency is due to dissipation in the acoustic boundary layer, which is a viscous effect that is not calculated in our simplified model where only first order pressure fields are considered [7].

| Material | Density, $\rho$ | Long. speed of sound, $c_L$ | Trans. speed of sound, $c_T$ | Bulk damping factor, $\Gamma$ |
|----------|-----------------|------------------------------|-------------------------------|-------------------------------|
| water | $998\,\text{kg m}^{-3}$ | $1497\,\text{m s}^{-1}$ | $1497\,\text{m s}^{-1}$ | $4.0 \times 10^{-3}$ |
| PYREX | $2230\,\text{kg m}^{-3}$ | $5592\,\text{m s}^{-1}$ | $3424\,\text{m s}^{-1}$ | $4.0 \times 10^{-4}$ |
| PDMS | $1028\,\text{kg m}^{-3}$ | $1019\,\text{m s}^{-1}$ | $32.2\,\text{m s}^{-1}$ | $8.9 \times 10^{-3}$ |

Table 4.1: Parameters at 25 °C used for simulations. $c_T$ for PDMS was calculated from $\rho$ and $c_L$ using equation (4.7). $\Gamma$ for PDMS was derived from the attenuation coefficient for $f = 3\,\text{MHz}$ [12]. The other parameters come from "*Fluid-solid coupling in COMSOL*" by Henrik Bruus [11].

### 4.1.3   Mesh

Having defined the primary system to be modelled and the corresponding boundary conditions, it is time to define the granularity of the mesh with which the simulations will be run. This is essentially the trade-off between computation time and accuracy or resolution. In order to find a suitable granularity we will perform a mesh convergence analysis. To do so, we define a mesh parameter $d_{bulk}$ to describe the size of the mesh elements, however since we expect a high divergence in the first order pressure field near the actuation region, we define a secondary parameter $d_{edge} = \frac{1}{2}d_{edge}$ to describe the element size on the boundary of the actuator. A visualisation of the mesh can be seen in the top of figure 4.2. The primary idea behind a mesh convergence analysis is to compare solutions to the fields of interest with decreasing mesh size parameter $d_{bulk}$ and ideally find the parameter value whereby a further decrease does not result in an improved solution. We hence define a relative convergence parameter $C(g)$ for a solution $g$ with respect to a reference solution $g_{ref}$, taken to be the solution with the lowest $d_{bulk}$ the computer is capable of computing [13],

$$C(g) = \sqrt{\frac{\int (g - g_{ref})^2 \mathrm{d}x\mathrm{d}r}{\int g_{ref}^2 \mathrm{d}x\mathrm{d}r}}. \tag{4.8}$$

As the computer used for simulating had $8\,\text{GB}$ of RAM, the lowest mesh size parameter was set to $d_{bulk} = 0.015R_2$ which corresponds to solving for 597091 degrees of freedom with a peak RAM usage of $3.62\,\text{GB}$ and a solution time of $18\,\text{s}$. In the bottom of figure 4.2 we see the convergence of all three fields develop similarly as the mesh size parameter $d_{bulk}$ is decreased, which is to be expected as they are all first order fields. Based on the figure, we have chosen a threshold of $C = 0.04$ thereby requiring a mesh granularity defined by $d_{bulk} = 0.052R_2$ in order for all fields considered in this thesis to abide to the threshold value, which will be implemented in all computations unless otherwise stated.

## 4.2   Validation

In the following section we intend to validate some of the results found in the theoretical section of this thesis, as to ensure that the simulations can be relied upon. Specifically we
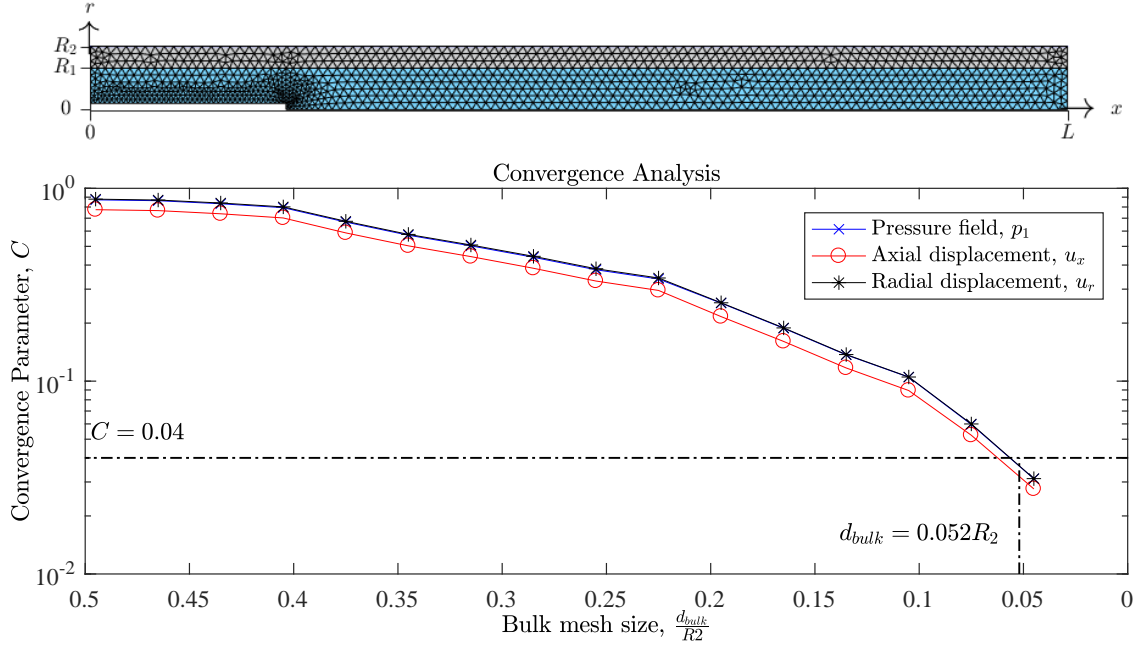
Figure 4.2: Top: A visualisation of the mesh for $h_{bulk} = 0.15R_2$. Bottom: A semi-logarithmic of the relative convergence parameter $C$ for the three primary fields of interest $p_1$, $u_x$ and $u_r$ as a function of decreasing mesh element size $d_{bulk}$. The horizontal dashed line indicates a threshold of $C = 0.04$ which was chosen as a trade-off between computational time and accuracy. To ensure that all fields come below this convergence threshold we require a mesh size of $d_{bulk} = 0.052R_2$ denoted by the vertical dashed line.

are interested in the validation of the axis-symmetric equations (3.17) and (3.24), as well as an investigation of the implementation of PML.

### 4.2.1 Helmholtz equation

Starting with the Helmholtz equation, the idea is to compare the simulated fields with an analytical solution to equation (2.29). In cylindrical coordinates we have,

$$\nabla^2 p_1 = -k_f^2 p_1 \;\Rightarrow\; \left(\partial_x^2 + \frac{1}{r}\partial_r(r\partial_r) + \frac{1}{r^2}\partial_\phi^2\right) p_1 = -k_f^2 p_1 \tag{4.9}$$

where we have used equation (3.13) to write the Laplace operator in cylindrical coordinates. The above equation can be solved by separation of variables. We assume that the pressure field can be written as,

$$p(x, r, \phi) = p_x(x)p_r(x)p_\phi(\phi), \tag{4.10}$$

where we have omitted time dependence and the subscript 1 for simplicity. Inserting equation (4.10) into equation (4.9) and dividing through by $p$ we get (where the explicit

dependence has been dropped),

$$\left(\frac{1}{p_x}\partial_x^2 p_x\right) + \left(\frac{1}{rp_r}\partial_r(r\partial_r p_r) + \frac{1}{r^2 p_\phi}\partial_\phi^2 p_\phi\right) = -k_f^2. \tag{4.11}$$

We see that the first set of parenthesis only depends on $x$ and the second set only depends on $r$ and $\phi$. The only way it is possible for these terms to be equal for arbitrary choices of $x$,$r$ and $\phi$ is if they are both equal to a constants. We denote the constants $-k_x^2$ and $-k_r^2$ respectively, such that $k_f^2 = k_x^2 + k_r^2$, giving the following two equations,

$$\frac{1}{p_x}\partial_x^2 p_x = -k_x^2 \quad \text{and} \quad \frac{1}{rp_r}\partial_r(r\partial_r p_r) + \frac{1}{r^2 p_\phi}\partial_\phi^2 p_\phi = -k_r^2. \tag{4.12}$$

Multiplying the second equation in equation (4.12) by $r^2$, we get a term that only depends on the angel $\phi$ and a term that only depends on $r$. Hence we can conclude that the angle dependent term must be equal to a constant which we denote $-k_\phi^2$, yielding the equation,

$$\frac{1}{p_\phi}\partial_\phi^2 p_\phi = -k_\phi^2. \tag{4.13}$$

We see that equation (4.13) and the first equation in equation (4.12) are the same type of equation with the following known solutions,

$$p_x(x) = Ae^{ik_x x} + Be^{-ik_x x} \quad \text{and} \quad p_\phi = Ce^{ik_\phi \phi} + De^{-ik_\phi \phi}, \tag{4.14}$$

where $A, B, C$ and $D$ are constants whose values depend on the given boundary conditions. Knowing that the pressure field has to be periodic in $\phi$, we have that $p_\phi(\phi) = p_\phi(\phi + 2\pi)$ which is only possible if $k_\phi = m$ where $m \in \mathbb{Z}$. Hence, the final equation to solve becomes,

$$r^2\left(\frac{1}{rp_r}\partial_r(r\partial_r p_r)\right) = -r^2\left(k_r^2 - \frac{m^2}{r^2}\right) \Rightarrow \frac{1}{rp_r}\partial_r(r\partial_r p_r) + \left(k_r^2 - \frac{m^2}{r^2}\right) = 0. \tag{4.15}$$

The general solutions to equation (4.15) are the cylindrical Bessel functions. Choosing to ignore the second kind Bessel function, the Neumann function $N_m$, which diverges at the origin, we get the following solution to the radial equation,

$$p_r(r) = EJ_m(k_r r) \tag{4.16}$$

where $J_m$ is the first kind Bessel function and $E$ is a constant. For a cylinder of radius $R_1$ and length $L$ we know from equation (4.1) that $p_1(L, r, \phi) = 0$, allowing us to simplify the expression for $p_x$ to (only considering outgoing waves, i.e. $B = D = 0$),

$$p_x(x) = \cos(k_x x) \quad , \quad k_x = \frac{n\pi}{L}, \tag{4.17}$$

where $n \in \mathbb{Z}$. The complete solution thereby becomes,

$$p(x, r, \phi) = \sum_n \sum_m p_{amp} J_m(k_r r)e^{im\phi}\cos(k_x x), \tag{4.18}$$

where $p_{amp}$ is the total combined constant [14]. As evident, we recover the assumption for the angle dependency applied in the derivation of the axis-symmetric equations where $m$ is the angular mode. Applying the hard-wall boundary condition $\boldsymbol{n} \cdot \boldsymbol{\nabla} p(x, R_1, \phi) = 0$ on the walls of the cylinder, we must require,

$$\partial_r J_m(k_r R_1) = 0 \; \Rightarrow \; k_r R_1 = \gamma_{mk}, \tag{4.19}$$

where $\gamma_{mk}$ is the $k$th root of the derivative of the Bessel function $J_m'$. The first couple of values are $\gamma_{01} = 3.8317$, $\gamma_{11} = 1.8412$ and $\gamma_{12} = 5.3314$. Knowing that $k_f^2 = k_x^2 + k_r^2$, we therefore get the resonance frequencies of the system to be,

$$\frac{\omega_{mk}^2(1 + i\Gamma_f)^2}{c_f^2} = \left(\frac{n\pi}{L}\right)^2 + \left(\frac{\gamma_{mk}}{R_1}\right)^2 \; \Rightarrow \; \omega_{mk} \approx c_f \sqrt{\left(\frac{n\pi}{L}\right)^2 + \left(\frac{\gamma_{mk}}{R_1}\right)^2}. \tag{4.20}$$

To check whether the derived weak-form Helmholtz equation can reproduce these analytical results, we defined a geometry in COMSOL with radius $R_1$ and length $L = 5\,\text{mm}$ and implemented hard-wall boundary conditions on the boundaries at $r = 0$ and $r = R_1$ and soft-wall boundary condition on the far end of the cylinder defined by $x = L$. The system was actuated with the following constraint,

$$p(0, r, t) = d_0 \left(1 + \frac{r}{R_1}\right) e^{-i\omega t}, \tag{4.21}$$

where $d_0 = 0.1\,\text{nm}$ as per usual. Since the Helmholtz equation only describes the first order field, it is necessary set the bulk viscosity damping factor to the calculated $\Gamma_f = 5 \times 10^{-6}$ rather than the physical $\Gamma_f$ found in table 4.1 caused by second order phenomena. If this is not done, the fields die too quickly, meaning that the expected Bessel resonances cannot be found visualised numerically. Starting with the $m = 0$ case, we expect the first resonance frequency to be $f_{01} \sim 2.148\,\text{MHz}$ using equation (4.20). Performing a frequency sweep near the expected resonance, we recovered a resonant solution at the frequency $f_{sim} = 2.149\,\text{MHz}$, a deviation of 0.05% from the expected frequency. As evident in figure 4.3, the simulated pressure field fully corresponds to the expected analytical solution, which together with the very small deviation from expected frequency seems to fully validate equation (3.17) as well as the modelling method introduced earlier in this chapter.

We perform a similar study for $m = 1$, where an additional boundary condition must be implemented. Due to the field having an angle dependency, the magnitude must go to zero on the axis as to ensure no discontinuities are created. For the first angular mode, we expect the first resonant frequency to be $f_{11} \sim 1.032\,\text{MHz}$, a frequency sweep in this region revealed a peak at $f_{sim} = 1.034\,\text{MHz}$, a deviation of only 0.19%. The simulated and analytical solutions to the pressure can be seen in figure 4.4 where it becomes evident that the simulated fields evolves completely as expected from theory.

### 4.2.2 Equation of motion

As there is no analytical solution to the displacement of an elastic solid in three dimensions, the best form of validation available is to compare results with a full three dimensional
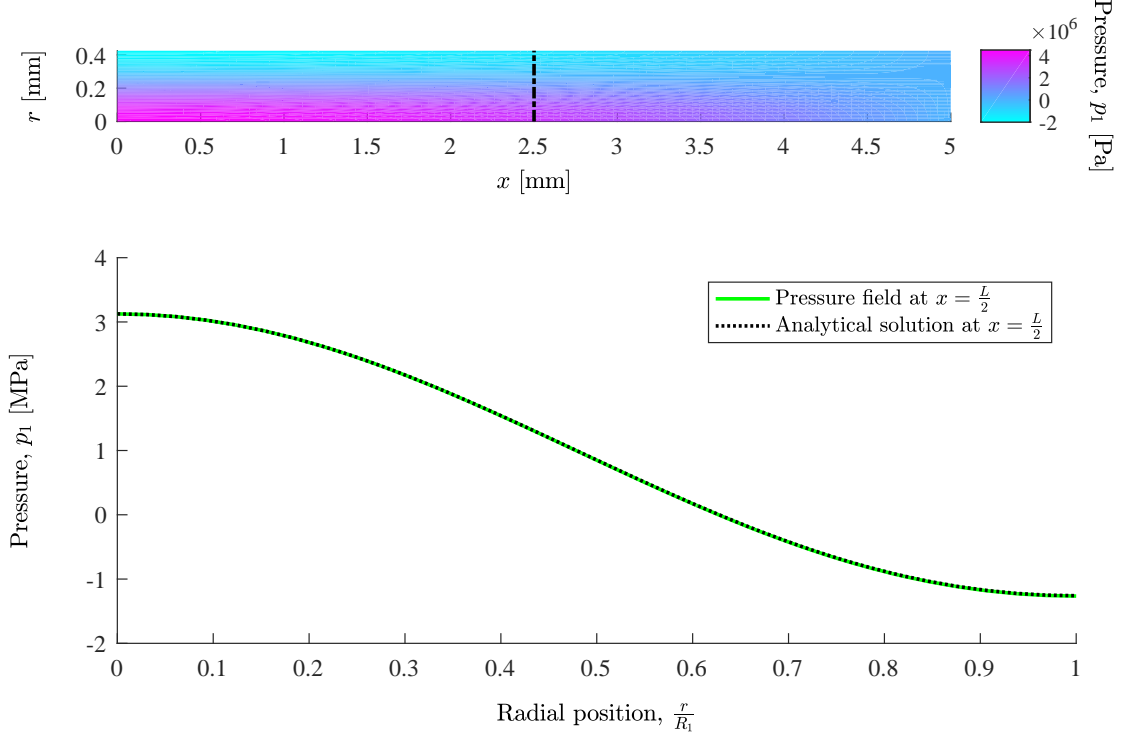
Figure 4.3: Top: Colour plot of the first order pressure field for angular mode $m = 0$ at frequency $f = 2.149\,\text{MHz}$. Bottom: The first order pressure for angular mode $m = 0$ field plotted as a function of the radial coordinate $r$ at axial position $x = 0.5L$ (the dotted line in the top figure). The green line shows the simulated pressure field, whilst the dotted line is the analytical solution to the Helmholtz equation with $p_{amp} = -1.259\,\text{MPa}$.

numerical solution. For the validation we consider a cylinder of radius $R_2$ and length $L = 5\,\text{mm}$ made of PYREX glass. The actuation will be done by a actuating band of length $\frac{1}{10}L$ wrapped around cylinder in one of the ends, which depending on which angular mode we are considering, will be actuated in different ways. The boundary conditions are the general zero-flux condition $\boldsymbol{n} \cdot \boldsymbol{\sigma} = \boldsymbol{0}$ on the boundaries with air for both the three dimensional model as well as the two dimensional one, a symmetry condition on the surface defined at $x = 0$, and the general symmetry condition on the axis for the two dimensional model alone, both given by $\boldsymbol{n} \cdot \boldsymbol{u} = 0$. Starting with $m = 0$, the actuation in the case of the two dimensional mode simply becomes,

$$\boldsymbol{u}(x, R_2, t) = d_0 e^{-i\omega t} \hat{\boldsymbol{e}}_r \quad , \quad 0 \leq x \leq \frac{1}{10}L. \qquad (4.22)$$

For the three dimensional model, it is necessary to transform the above actuation from cylindrical to Cartesian coordinates. This is done using the well known relation between
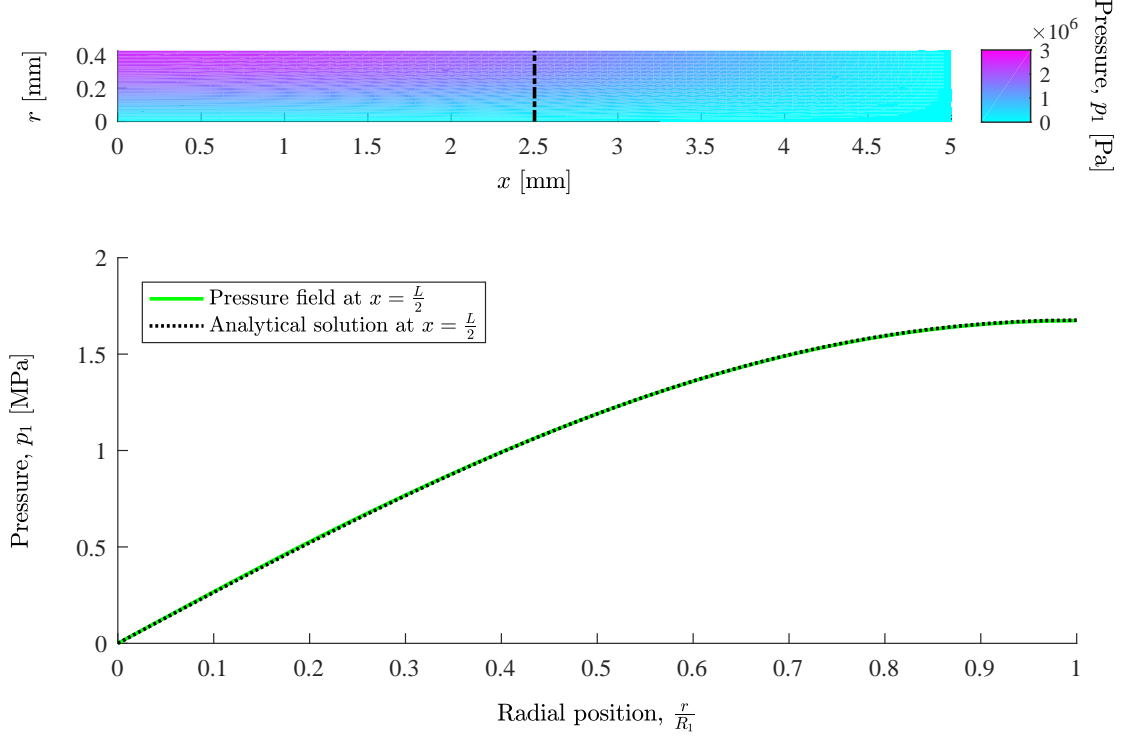
Figure 4.4: Top: Colour plot of the first order pressure field for angular mode $m = 1$ at frequency $f = f = 1.032\,\mathrm{MHz}$. Bottom: The first order pressure for angular mode $m = 1$ field plotted as a function of the radial coordinate $r$ at axial position $x = 0.5L$ (the dotted line in the top figure). The green line shows the simulated pressure field, whilst the dotted line is the analytical solution to the Helmholtz equation with $p_{amp} = 1.767\,\mathrm{MPa}$.

the two coordinate systems,

$$\begin{pmatrix} u_x \\ u_y \\ u_z \end{pmatrix} = \begin{pmatrix} 1 & 0 & 0 \\ 0 & \cos\phi & -\sin\phi \\ 0 & \sin\phi & \cos\phi \end{pmatrix} \cdot \begin{pmatrix} u_x \\ u_r \\ u_\phi \end{pmatrix}. \tag{4.23}$$

This yields the following actuation in Cartesian coordinates to be used in the three dimensional model,

$$\boldsymbol{u}(x, y, z, t) = d_0 \frac{y}{R_2} e^{-i\omega t} \hat{\boldsymbol{e}}_y + d_0 \frac{z}{R_2} e^{-i\omega t} \hat{\boldsymbol{e}}_z \quad , \quad 0 \leq x \leq \frac{1}{10} L \text{ and } y^2 + z^2 = R_2^2, \tag{4.24}$$

where we have used the fact that on the boundary $\cos\phi = \frac{y}{R_2}$ and $\sin\phi = \frac{z}{R_2}$. We then found a resonant frequency that was present in both simulations (the two dimensional model can only find axis-symmetric resonances, whilst the three dimensional model finds all resonances), and compared the two numeric solutions. In figure 4.5 we see the comparison of the three components of the displacement field in cylindrical coordinates, where the

results from the three dimensional model have been transformed using equation (4.23). Since we only look at $\phi = 0$ we have $u_x = u_x$, $u_r = u_z$ and $u_\phi = -u_y$. As evident, both the radial and axial components evaluated by the two dimensional model are very similar to the ones evaluated by the full three dimensional model. There is a small deviation in the angular component, this can be explained by the fact that the three dimensional model may have an overlap with an acoustic mode that is not axis-symmetric and hence the non-zero contribution. However, the deviation is very small when compared to the scales in the axial and radial components, and thus we can conclude that the model has been validated for $m = 0$. In order to validate equation (3.24) for $m = 1$ we need to find a way to actuate these modes in the three dimensional model. Knowing that $m = 1$ corresponds to a cosine angle dependence ($\mathrm{Re}(e^{i\phi}) = \cos(\phi)$), we can excite these specific modes by multiplying our previous actuation function with a cosine. Specifically we now have the following actuation,

$$\boldsymbol{u}(x,y,z,t) = d_0 \frac{y^2}{R_2^2} e^{-i\omega t} \hat{\boldsymbol{e}}_y + d_0 \frac{zy}{R_2^2} e^{-i\omega t} \hat{\boldsymbol{e}}_z \quad , \quad 0 \leq x \leq \frac{1}{10} L \text{ and } y^2 + z^2 = R_2^2, \quad (4.25)$$

where we once more have used the fact that $\cos\phi = \frac{y}{R_2}$. A similar study was performed where we found a resonant frequency in both models, and compared the displacements in a very similar manner. The results can be seen in figure 4.6. As evident, the radial and axial components are very similar when comparing across the models. However there is a huge deviation in the angular component. The reason for this significant deviation is unknown, and has thus been left as an unresolved issue that must be taken up by the Theoretical Microfluidics Group (TMF) at a later stage. Luckily, we have chosen to always use the angular mode $m = 0$ for all remaining results presented in this thesis. The reasons being partly due to the problem with the validation of equation (3.24) for $m > 0$, but also because it is easier in practice to actuate the $m = 0$ angular modes compared to the $m > 0$ modes, thus making the results gotten in the rest of the thesis more realistic.
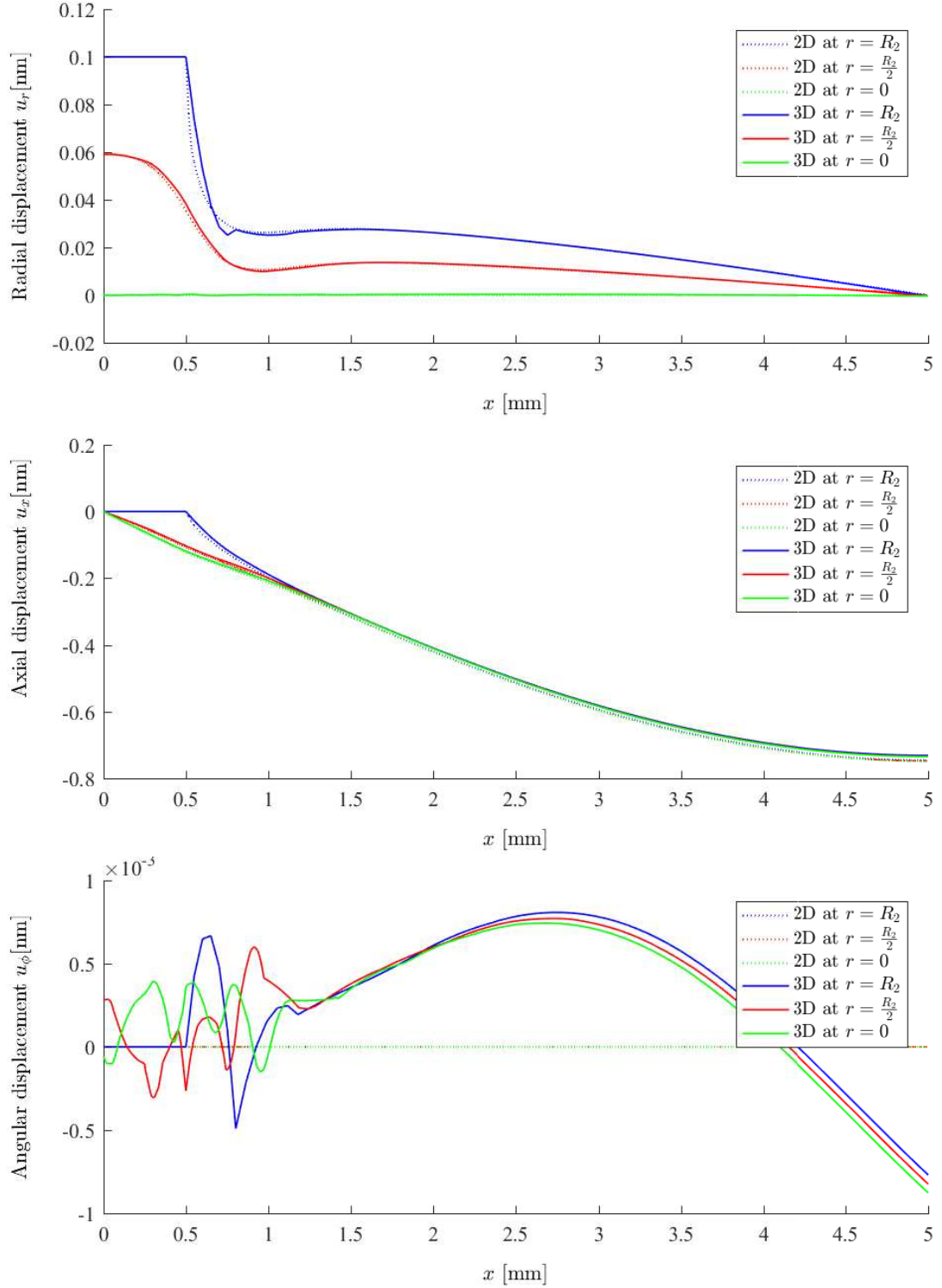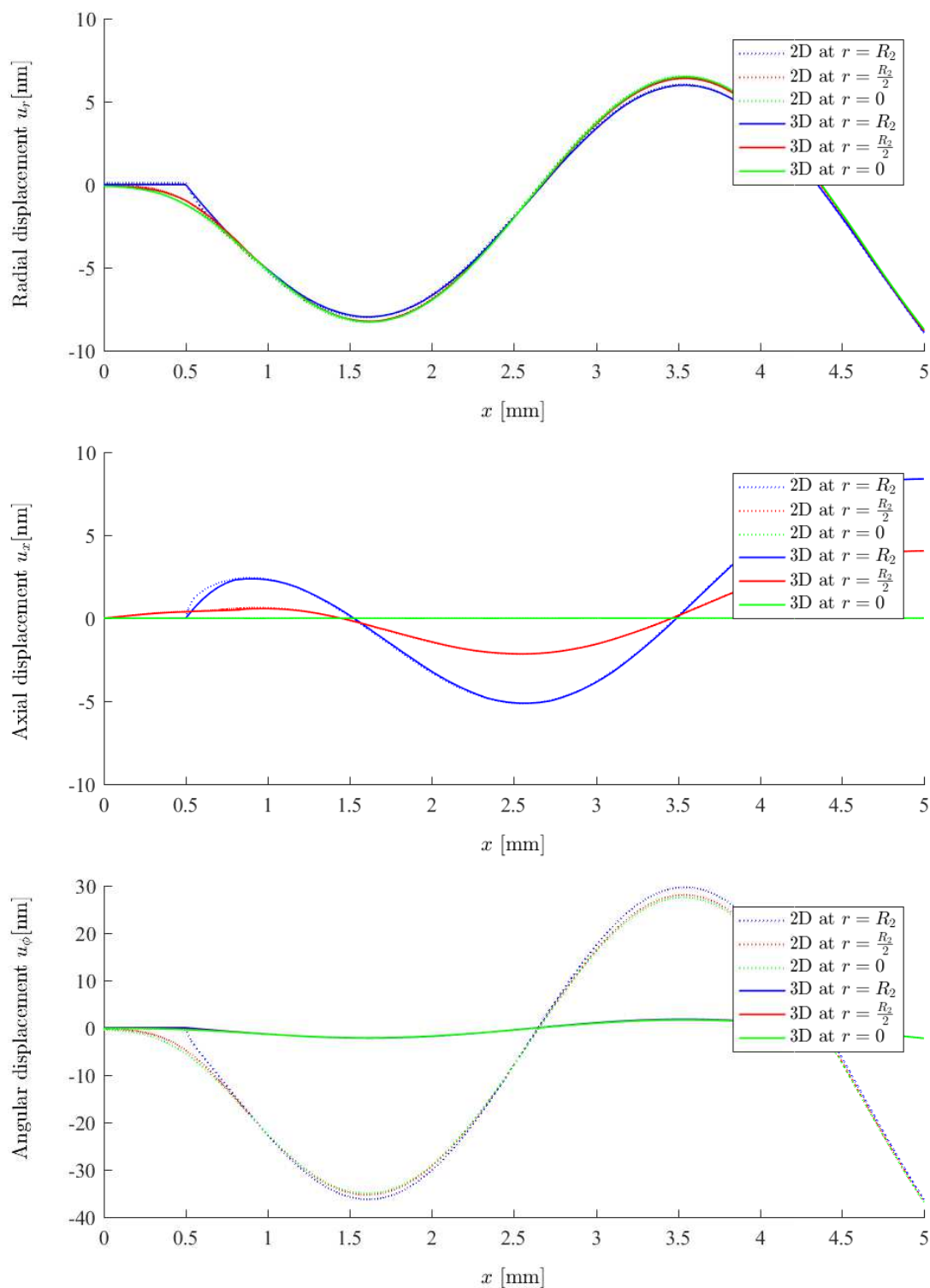
Figure 4.5: Top: Comparison of the radial component of the displacement field $u_r$ for $m = 0$ at three different radial positions $r = R_2, r = \frac{R2}{2}$ and $r = 0$ for $\phi = 0$ computed by the two dimensional model and the three dimensional model respectively. For the two dimensional model (dotted lines) the frequency used was $f_{2D} = 282.8539\,\text{kHz}$, for the three dimensional model solutions (solid lines) the frequency used was $f_{3D} = 284.3602\,\text{kHz}$. Middle: Comparison of the axial displacement $u_x$ under same conditions as for the radial displacement. Bottom: Comparison of the angular displacement $u_\phi$ under same conditions as for the radial and axial displacements.

Figure 4.6: Top: Comparison of the radial component of the displacement field $u_r$ for $m = 1$ at three different radial positions $r = R_2, r = \frac{R2}{2}$ and $r = 0$ for $\phi = 0$ computed by the two dimensional model and the three dimensional model respectively. For the two dimensional model (dotted lines) the frequency used was $f_{2D} = 529.255\,\mathrm{kHz}$, for the three dimensional model solutions (solid lines) the frequency used was $f_{3D} = 533.590\,\mathrm{kHz}$. Middle: Comparison of the axial displacement $u_x$ under same conditions as for the radial displacement. Bottom: Comparison of the angular displacement $u_\phi$ under same conditions as for the radial and axial displacements.

## 4.3 PML Testing

In the following section we intend to implement and explore a PML to the primary system described in the very beginning of this chapter. More specifically we will test how close to the source of actuation the PML can start without influencing the fields outside the PML region, and for which absorption parameters the PML successfully dampens the incident wave. The PML will be implemented as an extension to the primary system such that it starts at $x = L$ with a height of $R_2$ and a length of $L_{PML}$. To achieve the best results, $L_{PML}$ should be similar of length to the longest wave length in the system [6]. Assuming that we are running simulations at frequencies $f \sim 1\,\text{MHz}$ as to match the frequencies used in the laboratories [2], we get the longest wave length in the system to be that of the longitudinal wave in PYREX at,

$$\lambda_{max} = \frac{c_{L_{PYREX}}}{f} = \frac{5592}{1 \times 10^6} = 5.592\,\text{mm} \approx \frac{1}{2}L. \tag{4.26}$$

Hence we set $L_{PML} = \frac{1}{2}L$. The geometry as well as the damping effects caused by implementation of PML can can be visualised in figure 4.7. As evident, both the displacement and pressure fields quickly die once they enter the PML region, the start of which is marked by the dotted line.
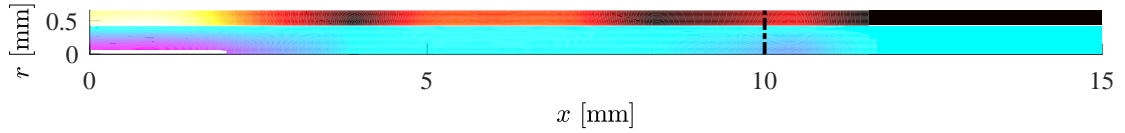


Figure 4.7: Colour plot of both the total displacement $\sqrt{u_x^2 + u_r^2}$ (hot) and the pressure field $p$ (cold) for the frequency $f = 1.55\,\text{MHz}$, a PML length of $L_{PML} = \frac{L}{2} = 5\,\text{mm}$ and an absorption strength of $k_{PML} = 100$. The dotted line represents the start of the PML region.

### 4.3.1 Absorption strength

In order to check for which values of $k_{PML}$ the incident pressure wave is fully dampened such that no traces of back scattering from the end of the region at $x = L + L_{PML}$ or from the start of the PML region at $x = L$ can be seen, we run a logarithmic parameter sweep of the absorption strength. The parameter was thus varied from $k_{PML} = 1 \times 10^{-5}$ to $k_{PML} = 1 \times 10^8$, and for each iteration the the pressure and displacement fields were evaluated at specific points in the acoustic chamber. Before the plots can be analysed it is necessary first to introduce the "acoustic energy" used for both the pressure and

displacement fields. Starting with the pressure field,

$$E_{ac} = \text{avg}\left[\frac{1}{2}\frac{p^2}{\rho_f c_f^2}\right] = \text{avg}\left[\frac{1}{2}\kappa_f p^2\right], \tag{4.27}$$

where $\kappa_f$ is the compressibility of the fluid and avg denotes an averaging operation done by COMSOL within the domain where the pressure field is defined. For the displacement field, the following expression was defined as a measure of the energy,

$$E_{ac} = \text{avg}\left[\frac{1}{2}\rho_s \omega^2 \sqrt{u_x^2 + u_r^2}\right]. \tag{4.28}$$

As to ensure any conclusions would be valid, we chose to monitor the acoustic energy $E_{ac}$ in three different points for each of the fields. A point in the actuator region $p_1$, a point in the channel $p_2$ and a point in the PML region $p_3$, defined in the figure caption. From figure 4.8 we can conclude that the range of $k_{PML}$ for which both the displacement field and the pressure field are fully dampened is for $1 \leq k_{PML} \leq 2 \times 10^5$. The reason we can conclude that the region of constant acoustic energy corresponds to the region of perfect damping lies in the development of the acoustic energy in the PML region, denoted by the green line in the plots. As evident, once the energies in the actuator region and chamber respectively begin to flatten out, the energy in the PML region drops to zero. This implies one of two things, either the wave is completely dampened once it enters the PML region, or it is completely reflected at the start of the PML region. However, if it was the case that the wave was completely reflected, we would expect the acoustic energy in the chamber (red line) to be comparable to when the parameter $k_{PML}$ is very small, however we see it drop significantly implying that we have perfect damping. The reason we expect the energy to be comparable if the wave were reflected is because for small values of $k_{PML}$ the wave practically propagates unaffected through the PML region and reflects at the far end, which is what is seen in both graphs for $k_{PML} < 1$. For higher $k_{PML}$ we begin to see the acoustic energy fluctuate, implying that the absorption strength is now so large that the transition is too extreme for the wave to enter the PML region and is thus reflected instead. For the rest of this thesis we will therefore be applying an absorption strength of $k_{PML} = 100$ whenever PML is implemented, unless otherwise stated.

### 4.3.2   Distance from actuator

Having found that the range of absorption strength is very large and thereby not a parameter to be careful about when implementing PML (given that the results are insensitive to $k_{PML}$ when within the range), we now have investigate how close to the actuation we can place a PML without it having consequences on the resulting fields outside the PML region. To do this we evaluated the fields for different device lengths $L > L_{act}$, the results of which can be seen in figure 4.9. From the figure we see that the shorter the device length, or rather the closer the PML region is to the region of actuation, the more the fields deviate from the true unaffected field, i.e. the field for $L = 8\,\text{mm}$. We also notice that the PML region has no impact on the field within the channel when $x > 5\,\text{mm}$. A

reason for this could lie in the hypothesis that the wave needs to have undergone a full oscillation after actuation before it can be dampened without any influence on the field for $x < L_{PML}$. This matches well when recalling that the longest wavelength of the system was $\lambda_L \approx 5.5\,\mathrm{mm}$. Hence, we can conclude that a length of $L = 10\,\mathrm{mm}$ is long enough to ensure that the implementation of a PML region has no impact on the fields for $x < L_{PML}$.
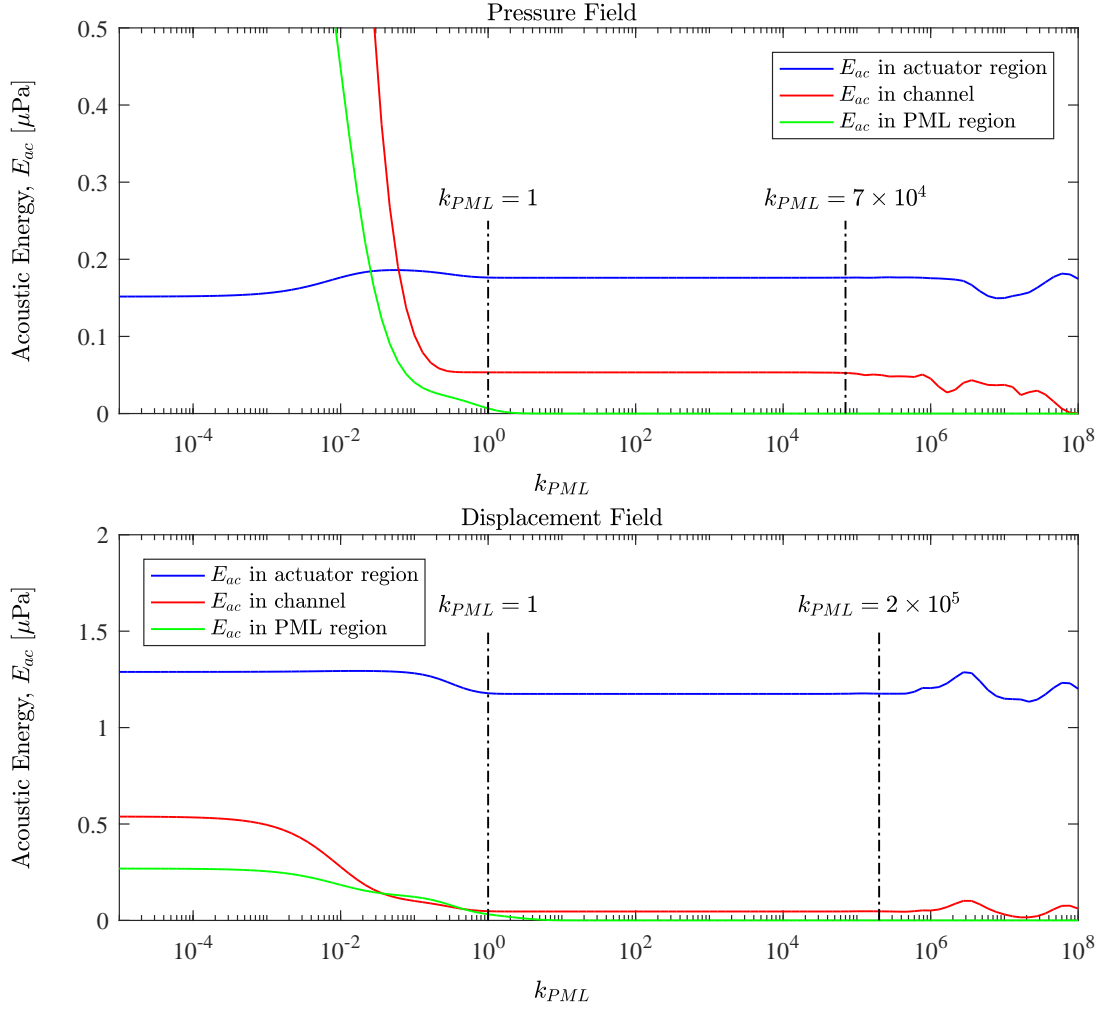
Figure 4.8: Top: The acoustic energy of the pressure field $E_{ac}$ in the chamber plotted as a function of varying absorption strength $k_{PML}$ for three different points in the system. The points were defined as, the actuator region $p_1 = (0.5L_{act}, 0.5R_1)$, the channel $p_2 = (0.75L, 0.5R_1)$ and the PML region $p_3 = (L + 0.5L_{PML}, 0.5R_1)$. The dotted vertical lines at $k_{PML} = 1$ and $k_{PML} = 7 \times 10^4$ represent the range for which $E_{ac}$ is constant and thereby the range for which we have perfect absorption. Bottom: A similar plot for the displacement field. The points were defined as, the actuator region $p_1 = (0.5L_{act}, 0.5(R_1 + R_2))$, the channel $p_2 = (0.75L, 0.5(R_1 + R_2))$ and the PML region $p_3 = (L + 0.5L_{PML}, 0.5(R_1 + R_2))$. The vertical lines at $k_{PML} = 1$ and $k_{PML} = 2 \times 10^5$ represent the range for which the energy is constant and thereby the range for which we have perfect absorption.
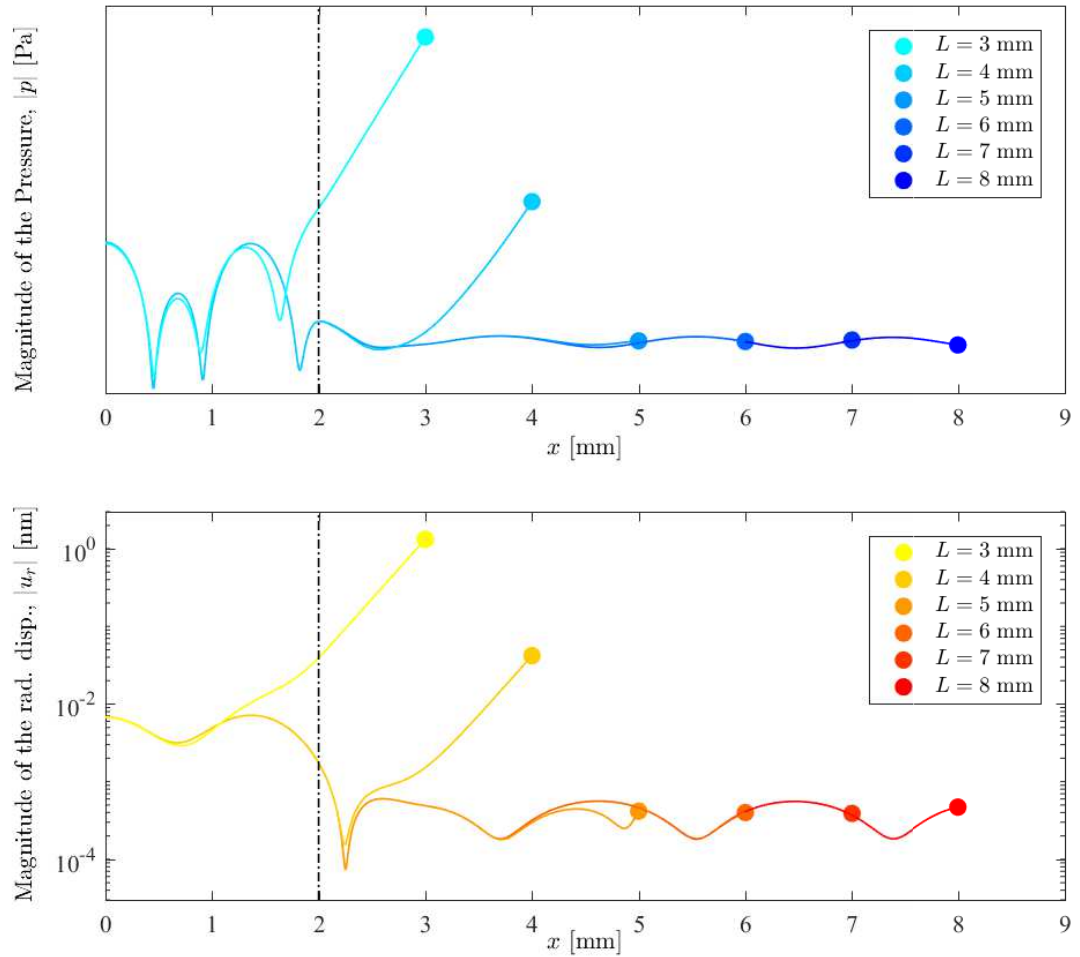
Figure 4.9: Top: Magnitude of the pressure field $|p|$ at $r = \frac{1}{2}R_1$ as a function of the axial position $x$ for different device lengths $L$ with a fixed PML region with length $L_{PML} = 5\,\text{mm}$ placed at $x = L$. The pressure was measured along the $r = 0.5R_1$ line. The vertical line represents the end of the actuator region. Bottom: A similar plot for the magnitude of the radial part of the displacement field $|u_r|$. The displacement was measured along the $r = 0.5(R_1 + R_2)$ line. The vertical line represents the end of the actuator region.

# Chapter 5

# Results

In the following chapter, we shall investigate the impacts of using rubber tubes to pump water in and out of the acoustic devices. Specifically we will be investigating two different types of material damping known as free layer damping and constrained layer damping respectively [15]. After this, we will explore the impacts that materials with linearly varying densities might have on the pressure field.

## 5.1 Impact of Polydimethylsiloxane (PDMS)

As a starting point we assume that the material used for the transportation of water into the chambers is made of polydimethylsiloxane (PDMS), a silicone based rubber. The reason for assuming this, is that it is frequently used to build micro-fluidic devices, and hence its material properties are well known as evidenced in table 4.1. In order to evaluate the impact of having a layer of PDMS around the ends of the cylindrical device we introduced in Chapter 4, it is necessary to investigate the device with no damping and with full damping. The latter will be simulated using PML as introduced in Chapter 3.

### 5.1.1 The no-damping and full-damping cases

As mentioned, we start our investigation by creating reference solutions representing a completely undamped device allowing for many internal reflections and a perfectly damped device where no reflections occur at the far ends of the device. However, before we can do this, it is first necessary to find a common system resonance, such that we ensure the solutions are comparable. To do this we consider the geometries introduced in figure 4.1 for the undamped system and the geometry explained in figure 4.7 for the damped system, and then simulate the acoustic energy of the pressure field defined in equation (4.27) for different frequencies. More specifically, we implemented a frequency sweep starting at $f = 0\,\mathrm{MHz}$ and ending at $f = 5\,\mathrm{MHz}$, in steps of $50\,\mathrm{kHz}$. The results can be seen in figure 5.1. As evident the black line representing the system without damping has a lot more spikes compared to the smooth blue line representing the system with PML. The reason for this lies in the fact that the undamped system will have all the standing-wave resonances caused by internal reflections in the $x$ direction, which are exactly the ones
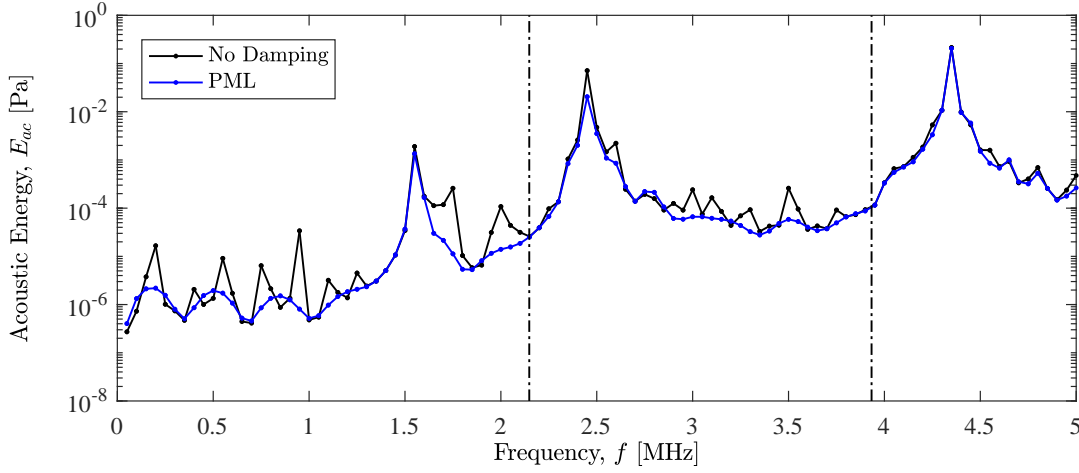
Figure 5.1: Plot of the acoustic energy density of the pressure field $E_{ac}$ as a function of the frequency $f$. The black line represents the results for the undamped system, the blue line represents the system perfectly damped by addition of a PML. The two dotted vertical lines correspond to the first two resonance frequencies for the Helmholtz equation, evaluated on the basis of equation (4.20) for $n = 0$ and $k = 1, 2$.

killed by the PML. Another interesting note lies in the fact that there seems to be three primary resonances within the system that appear for both the damped and undamped systems, specifically at $f \approx 1.5\,\mathrm{MHz}$, $f \approx 2.5\,\mathrm{MHz}$ and $f \approx 4.5\,\mathrm{MHz}$. As described in the caption, the dotted lines represent the first two resonance frequencies of the Helmholtz equation for the pressure. Intuitively one would think that the resonances should align with the specified peaks, however, we experience a shift which could be due to the fact that the liquid domain is coupled through the fluid-solid boundary condition (equation (4.3)) rather than the hard-wall boundary condition which forms the basis of the resonances marked by the dotted lines. In the following we shall compare the solutions to the two above-mentioned systems as well as the system to be described where we implement a PDMS tube, at the common resonance at $f = 1.560\,57\,\mathrm{MHz}$ (the exact number comes from closer inspection of the undampened solution).

### 5.1.2   Geometry

In order to model the tubes, we add a rectangle of height $h_m$ and length $L_m$ on top of the glass capillary in the far end of the geometry described in figure 4.1. Specifically for the described geometry the tube starts at $x = L - L_m$ and $r = R_2$. However, from some initial runs of the model with this new geometry having implemented the correct parameter values (from table 4.1), it was noticed that the displacement field in the PDMS region of the geometry was very discrete implying that the mesh parameter $d_{bulk} = 0.052R_2$ was not granular enough to describe the field within the PDMS. To solve this, given that we have a limit of 8 GB RAM, it was necessary to rebuild the mesh in such a way that the

mesh element size in the glass and fluid were increased as to allow for a more granular mesh in the PDMS region. The applied mesh can be visualised in the top of figure 5.2.
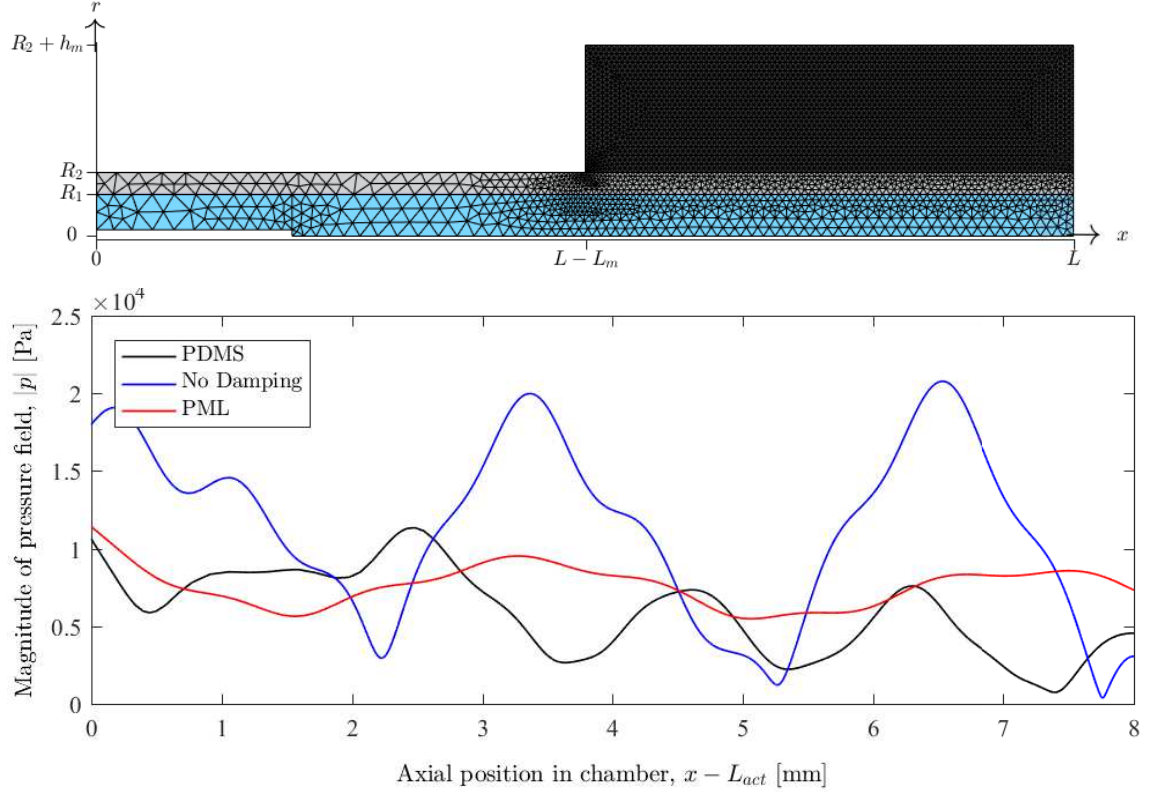


Figure 5.2: Top: A visualisation of the rebuilt mesh for the geometry with incorporated PDMS layer. The mesh parameters have been scaled with a factor 4 as to allow for inspection. Bottom: Plot of the magnitude of the pressure field $|p|$ along the line $r = 0.5R_1$ for three different systems as a function of the axial position within the chamber region. We are only plotting in the chamber region, since this is the area of interest concerning whether or not the displacement and pressure waves are travelling or standing. The three systems plotted for are the undamped system (blue line) at $f = 1.5606\,\text{MHz}$, the PML system (red line) at $f = 1.5696\,\text{MHz}$ and the PDMS (system) at $f = 1.5705\,\text{MHz}$.

### 5.1.3 Standing Wave Ratio (SWR)

In the bottom of figure 5.2 we see a comparison of the solution to the three systems. Where $h_m = 2R_2$ and $L_m = 0.5L$ are estimated from the experimental picture shown in figure 1.1. However, before we can compare the three systems, we need a way to characterise the amount of damping in the system. For a fully damped system, we expect only travelling waves at the resonance frequency, since all reflections will be killed by the damping. On the other hand we expect for the acoustic waves to be standing in the case of no damping,

since there is no mechanism to absorb the energy of the waves and hence there will be 100% reflection on the boundaries. In general we have for standing waves that the intensity over a full period of the wave is periodic with position with a given maximum and a minimum of zero due to the existence of nodes where the amplitude is zero at any given time. On the other hand, a purely travelling wave will have a constant intensity over a full period. Knowing this, we will introduce a measure, the standing wave ratio (SWR), to characterise the degree to which an arbitrary wave is a standing wave and thereby the degree to which the system is undamped. We define the ratio for a general acoustic wave denoted $v$ as follows,

$$\text{SWR} = \frac{\max\left[\langle|v|\rangle\right]}{\min\left[\langle|v|\rangle\right]}, \tag{5.1}$$

where $\langle v \rangle$ denotes the time average over a full period of the absolute value of the field (since the intensity is proportional to the square of the field amplitude, the same conclusions hold for the amplitude itself). We see that for a completely standing wave the ratio tends to infinity, meanwhile for a purely travelling wave the ratio becomes 1, implying that the range of the measure is $\text{SWR} \in [1, \infty]$ and the larger SWR is, the more standing the wave is and the more undamped the system is. With a measure established, we return to the bottom of figure 5.2 and evaluate SWR for the three systems,

$$\begin{aligned} \text{SWR}_{\text{PDMS}} &= \frac{11348}{745} \approx 15.23 \\ \text{SWR}_{\text{No Damp}} &= \frac{20779}{373} \approx 55.71 \\ \text{SWR}_{\text{PML}} &= \frac{11426}{5482} \approx 2.08. \end{aligned} \tag{5.2}$$

As expected, the system with the lowest SWR and thereby highest damping is the one with PML where all reflections in the $x$ direction are killed, whilst the system without any damping has the highest SWR. Interestingly, the system with the PDMS seems to have a significantly lower SWR than the system without damping which implies that the PDMS tube seems to have a damping effect on the system. The reason it seems as though the damping in the PDMS is higher from figure 5.2 at the end of the chamber, is due to the fact that the PDMS overlaps the chamber whilst all the damping in the case of the PML occurs after $x = 8\,\text{mm}$.

### 5.1.4   Free Layer Damping

The method of placing a layer of damping material on top of a vibrating system is generally known as free layer damping [15]. This method works on the principle that the vibrational energy from the glass chamber is transmitted to the damping material, which in our case would be the PDMS layer, where after it is dissipated due to the higher bulk damping factor compared to PYREX (see table 4.1). The choice of dimensions for the results represented in figure 5.2, although estimated from the basis of a photo from an actual laboratory, were somewhat arbitrary. In other words we have no idea how volatile the SWR calculated for the system in equation (5.2) is to changes in the geometry of the

PDMS region. We therefore continue our investigation of PDMS with a dimension sweep, where we vary the height $h_m$ from 1 to 8 glass widths, $h_g = R_2 - R_1 = 0.225\,\text{mm}$, in steps of 1 $h_g$, and the length $L_m$ from 1 mm to 8 mm (right at the end of the actuator region) in steps of 1 mm, and calculate the SWR for every combination. To do this, the mesh parameter was increased once more as to allow for the larger PDMS region ($h_m = 5h_g$ and $L_m = 8\,\text{mm}$). The results can seen in figure 5.3. As evident, the SWR is
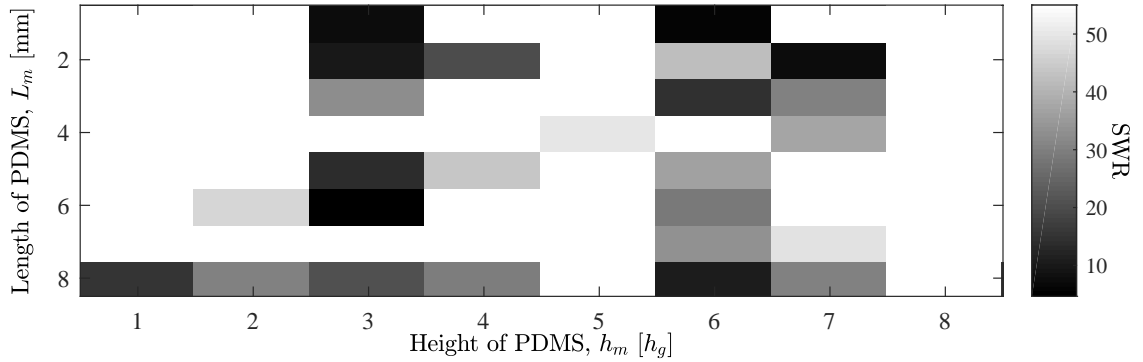


Figure 5.3: A matrix plot showing the SWR for all combinations of $L_m$ from 1 mm to 8 mm in steps of 1 mm and $h_m$ from 1 $h_g$ to 8 $h_g$ in steps of 1 $h_g$ for the single layer damping system. The scale has been capped at 55 as this is the SWR corresponding to the system with no damping.

very sensitive to changes in geometry and it seems that the height of the PDMS region is the most significant parameter in terms of obtaining maximum damping. Specifically we notice that heights $h_m = 3h_g$ and $h_m = 6h_g$ in general seem to produce the most damping and the lowest SWR was measured at $h_r = 3h_g$ and $L_m = 6\,\text{mm}$ to be 4.64, which is significantly lower than the 15.23 gotten from the first iteration, but not as effective as the PML layer. However, contrary to expectations, the damping does not increase regularly with the height of the PDMS layer. This might have something to do with the resonances in the PDMS. The energy from the acoustic wave in the PYREX glass can more easily be transferred to the PDMS layer, if the frequency matches a resonance frequency in the PDMS layer which very much depends on the height of the PDMS layer. Another interesting note from figure 5.3, is the fact that the PDMS seems to dampen a lot more if placed right after the actuator region (when $L_m = 8\,\text{mm}$). This intuitively makes sense since the acoustic wave has no chance to propagate freely before being absorbed by the PDMS layer. Another point is that by having the PDMS start right there is only a single abrupt change in acoustic impedance between the PDMS and the actuator region, skipping the abrupt change from the free chamber to the start of the PDMS region for

when $L_m < 8\,\mathrm{mm}$. Acoustic impedance $Z$ for a one dimensional wave is defined as

$$Z = \frac{\rho c}{A}, \tag{5.3}$$

where $\rho$ is the density of the material in which the acoustic wave is propagating, $c$ is the speed of sound and $A$ is the cross-sectional area through which the wave is travelling. Hence, we have abrupt changes when $A$ is suddenly increased, as is the case at the start of the PDMS layer. The reason changes in acoustic impedance are of importance, is due to the fact that the higher the change the more reflection implying a higher chance of generating standing rather than travelling waves.

### 5.1.5   Constrained Layer Damping

Free layer damping is not the only type of damping method out there involving the application of materials with damping properties. The other main type of damping that falls within such a category is constrained layer damping [15]. Constrained layer damping is based on the idea of adding a stiff material (PYREX glass) on top of the damping material (PDMS layer) which as with free layer damping is placed on top of the system we are interested in damping. This method is typically recommended for the damping of stiff materials, since the PYREX layer on top of the PDMS forces the damping of shear waves (the dominant type of wave in stiff materials), due to the fact that vibrations in the $r$ direction are constrained. The implementation of this type of damping to our modelling system was done by adding a layer on top of the PDMS layer from previous simulations with the same material parameters as the PYREX glass of length $L_m$ and height $h_g$. A similar investigation was then done where the parameters $L_m$ and $h_m$ were varied in the same way as was done to obtain the results in figure 5.3. Doing this leads to the results displayed in figure 5.4, which also gives a visual representation of the constrained layer damping mechanism with an overlapping mesh. As evident, we generally see an increase in damping the thicker the PDMS layer becomes. Specifically we obtain the lowest SWR equal to 5.28 at $h_m = 6h_g$ and $L_m = 1\,\mathrm{mm}$, which is higher than for the free layer damping. However, there are many more dark elements in figure 5.4 compared to figure 5.3, implying that in general constrained layer damping is more effective with respect to generating travelling waves for a larger span of geometries.

### 5.1.6   Extended Region

In the results above, we have only considered systems which end in a boundary with the surrounding air at $x = L$. However, in the experiments outlined in various articles [3][4][5], the rubber tubes are responsible for transporting the fluid into the acoustic chambers, and thus in reality it is not an air boundary, but rather a continuation of the fluid enclosed by a rubber layer rather then glass. The basic geometry can be seen in the top of figure 5.5 for the simple free layer damping, where the parameter $L_{ext}$ is used to describe the length of the rubber tube that extends beyond the glass channel. To investigate the effects of including the more realistic geometry, we measured the SWR for various values of $L_{ext}$ the results in the case of both free layer and constrained layer damping. The
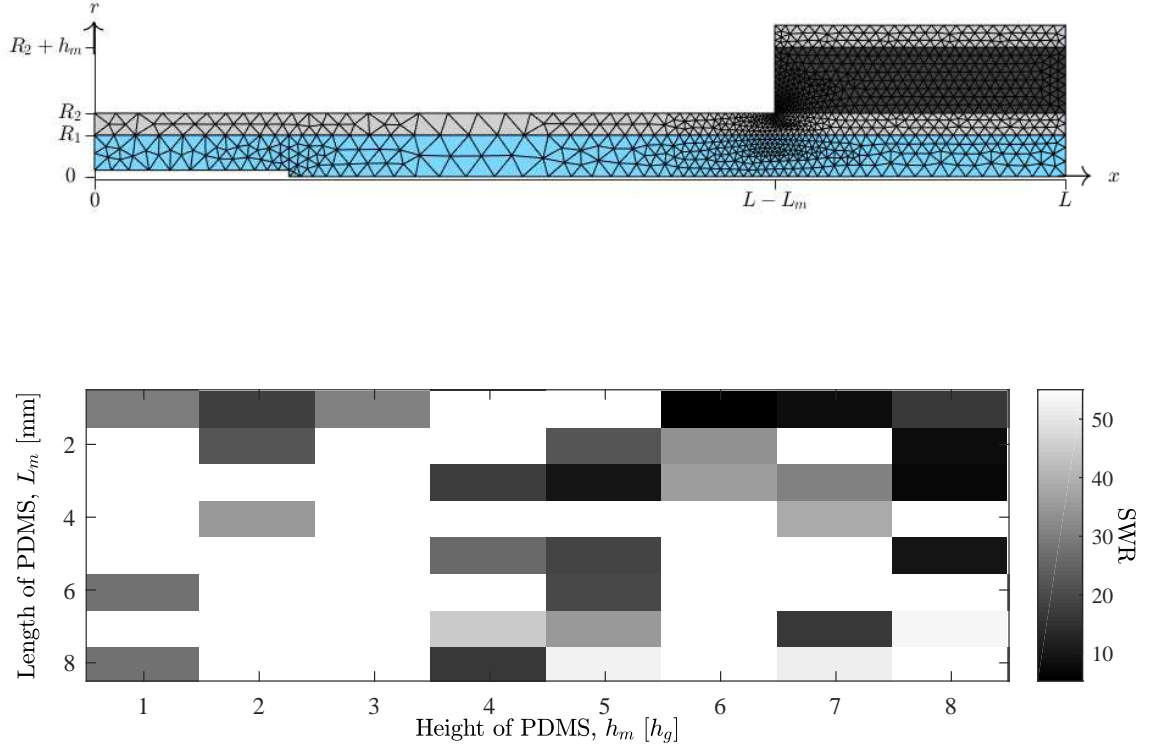
Figure 5.4: Top: A visualisation of the rebuilt mesh for the geometry with the constrained layer damping mechanism. The mesh parameters have been scaled with a factor 4 as to allow for inspection. Bottom: A matrix plot showing the SWR for all combinations of $L_m$ from 1 mm to 8 mm in steps of 1 mm and $h_m$ from 1 $h_g$ to 8 $h_g$ in steps of 1 $h_g$ for the constrained layer damping system. The scale has been capped at 55 as this is the SWR corresponding to the system with no damping.

specific dimensions of the PDMS layers which are to be extended have been chosen on the basis of figures 5.3 and 5.4 as the geometries with the lowest SWR. Specifically this implies $h_m = 3h_g$ and $L_m = 6\,\text{mm}$ for the free layer damping system and $h_m = 6h_g$ and $L_m = 1\,\text{mm}$ for the constrained layer damping system. The results can be seen in the bottom of figure 5.5. Firstly we notice that the SWR is significantly higher for small $L_{ext}$ compared to when we just had a fluid-air boundary at $x = L$. The reason for this could be related to the sudden change in acoustic impedance (defined in equation (5.3)) experienced when the cross sectional area of the fluid domain increases in size as the pyrex glass region ends at $x = L$. A sudden change in acoustic impedance generally leads to reflections thereby increasing the measured SWR. For larger values of $L_{ext}$ we see two very different phenomena for the two types of damping. For the free layer damping, we simply experience random fluctuations in the measured SWR which seems to imply that the geometry that caused the lowest SWR in the original geometry with the simple
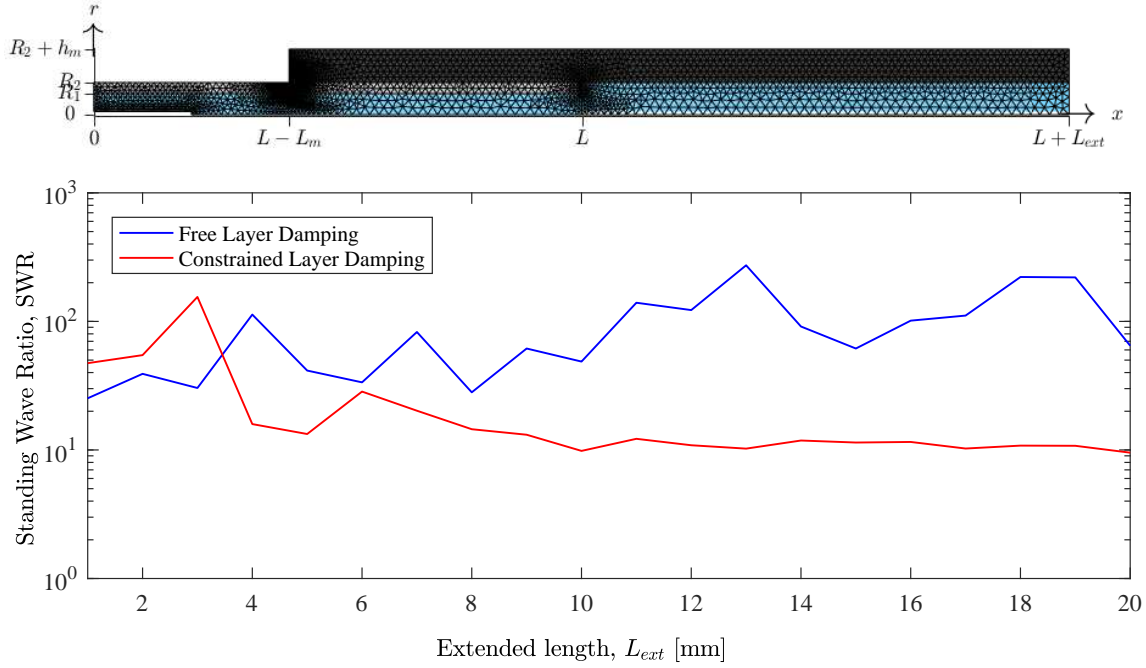
Figure 5.5: Top: A visualisation of the mesh for the geometry with the extended free layer damping. Bottom: Plot of the SWR as a function of varying tube lengths, denoted by $L_{ext}$, for both the system with free layer damping (blue line) and constrained layer damping system (red line). The general parameters of the damping mechanisms have been set to be the ones which resulted in the lowest SWR in figures 5.3 and 5.4.

fluid-air boundary, does not yield any minimum SWR when the geometry is extended beyond the glass capillary. The fact that the length does not impact the SWR also points towards the earlier conclusion drawn from figure 5.3 where we stated that it was the height $h_m$ rather than the length $L_m$ that impacted the damping of the system, and thereby the SWR, mostly. For the constrained layer damped system, we see that after some initial fluctuations for low $L_{ext}$, the SWR seems to drop to a significantly lower value where after it slowly continues to drop with increasing $L_{ext}$. The reason for the fluctuations in the start, could be due to the same reasons as that of the fluctuations evident for low channel distances in figure 4.9, namely that the longest acoustic wave present in the system $\lambda_{max} \approx 5.6$ mm has not undergone a full oscillation. The dropping SWR after initial fluctuations seems to imply that the longer the constrained damping mechanism becomes, the higher the damping effect. However, the lowest SWR is only 9.52 at $L_{ext} = 20$ mm which is significantly higher than the 5.28 achieved without extension which implies that the reflection caused by the change in impedance increases the SWR more than the extension can decrease it.

## 5.2 Optimizing Damping Effects

In the following section, we investigate the possibilities of achieving fully travelling waves through material manipulation which may or may not be experimentally feasible.

### 5.2.1 Varying Density

In the following section we attempt to achieve the lowest possible SWR by linearly varying the density in the material the capillary is made of. Specifically we fix the density at the centre of the entire capillary, i.e. at $x = 0$, to be equal to the density of PYREX glass as per usual. We then define a end density, denoted $\rho_{end}$, as the density at the ends of the capillary, i.e. at $x = L$. In COMSOL, we then implemented a function such that the density of the material varied linearly from $\rho_s$ (density of pyrex glass) at $x = 0$ to $\rho_{end}$ at $x = L$. In figure 5.6, we see the measured SWR for the acoustic pressure waves when varying the end density $\rho_{end}$ from $500\,\mathrm{kg\ m^{-3}}$ implying a decreasing density as $x$ increases, to $4500\,\mathrm{kg\ m^{-3}}$, implying a increasing density as $x$ increases. The reason this
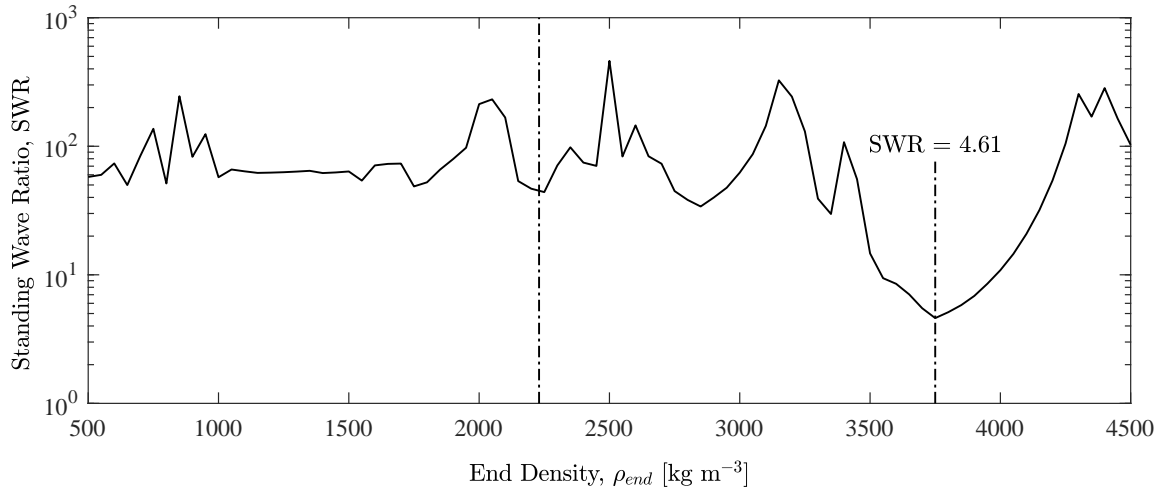


Figure 5.6: A plot of the SWR as a function of the end density $\rho_{end}$. The large vertical line represents the original density of the material $\rho_s = 2230\,\mathrm{kg\ m^{-3}}$. The small vertical line represents the minimum SWR achieved (4.61), which occurs at a end density of $\rho_{end} = 3750\,\mathrm{kg\ m^{-3}}$

might yield results, even when we are not altering the bulk damping factor $\Gamma$, is due to the fact that the longitudinal and transverse speeds of sound in the material, denoted $c_L$ and $c_T$ respectively, depend on the density of the material (see equation (4.7)). Hence, it is expected that the larger the end density $\rho_{end}$ compared to $\rho_s$ the more stiff the material becomes and thus the more dampened the acoustic waves become. As evident from figure 5.6, we see that the SWR is high for end densities lower than the original density which is to be expected since it only allows for wilder fluctuations in the ends as the density is lower and thus the material softer. On the other hand for higher end densities we find

a region from $\rho_{end} = 3500\,\text{kg m}^{-3}$ to $\rho_{end} = 4000\,\text{kg m}^{-3}$ where the SWR is very small which as mentioned above was to be expected. The lowest value achieved was SWR=4.61 which occured at $\rho_{end} = 3750\,\text{kg m}^{-3}$, which is on par with the lowest SWR achieved for the layer damping methods however still far from the optimal damping achieved by implementation of PML. It is however important to remember that these results are based on the assumption that when the density of the material is changed, it has no impact on any of the other fundamental material parameters, i.e. the Young's modulus $E$, Poisson's ratio $\nu$ and the bulk damping factor $\Gamma$. This is far from true, but since we have no expression for how the Young's modulus and Poisson's ratio change with density, and since we rely on experimental results for the bulk damping factors, it is the best we can do.

# Chapter 6

# Conclusion and Outlook

In this thesis we have studied how the rubber tubes used to control flow rates in acoustic trapping devices impact the acoustic pressure field. The motivation for doing this was that the first order acoustic pressure field has a direct impact on the strength of the trap (recall equation (1.1)). Our aim was thus first to develop the numeric capabilities required to investigate longer geometries since full three dimensional modelling would require to much computation time. Secondly, our aim was then, by use of these capabilities, initialize an investigation into how the rubber tubes could have an impact on the acoustic fields.

## 6.1 Conclusion

In order to reduce computation time, we chose to consider axis symmetric geometries, as this allowed for a simplifying assumption with respect to the angular coordinate. Application of this assumption then led to the reformulation of the wave equations for the pressure and displacement fields in a two dimensional form rather than their original full three dimensional forms. In our validation of these results, we concluded that the equation for the pressure field was very closely aligned with theory for angular modes. On the other hand, for the displacement field we could only fully validate the reduced equation for the 0th angular mode. The 1st angular mode seemed to cause problems in the angular component of the displacement field, which will have to be reviewed in another setting.

We then continued with the investigation of rubber tubes that were attached on the ends of the acoustic device. To quantify the effectiveness of the damping generated by tubes, a measure called the standing wave ratio was introduced, and in an initial simulation it was found that the PDMS tubes did indeed have a significant damping impact on the acoustic device. However, further investigation showed that the effects were very volatile to changes in geometry, and thus it became hard to draw any general conclusions other than it seemed as though the thicker the tube the greater the damping. An extension of the tubes to beyond the glass capillary introduced us to the problems of reflections caused by changes in acoustic impedance which seemed to play a large role in the transition from glass to PDMS.

Finally, we attempted to optimize damping effects by considering a material with linearly

varying density. It was found that there exists a small window where the acoustic pressure waves become largely travelling. This is an interesting result as the increased density does not result in increased damping, rather it would seem that the oscillations simply become travelling rather than standing.

## 6.2   Outlook

In the following section we highlight the various improvements and relevant ideas regarding the work done in the thesis which there simply was no time to incorporate.

### 6.2.1   Failure to validate reduced wave equation for elastic solids

As previously mentioned, there were issues in the validation of the dimension reduced elastic wave equations which naturally opens up to further investigations. The interesting point was that there were only issues with the angular component. Hence a clever starting point for this investigation would be to review the transformations done for this component.

### 6.2.2   Reduction of acoustic impedance

Also previously mentioned, the extension of the PDMS tubes beyond the glass capillary led to increased SWR rather than the expected decrease. It was hypothesised that the reason for this was the sudden change in acoustic impedance experienced by the pressure field at the boundary. Thus to avoid this complication, a linear transition could be made as to ensure a slow continuous development of the acoustic impedance.

### 6.2.3   Computational power

Although we successfully managed to reduce the computational power required to model the acoustic devices, it was found that, due to the limited amount of RAM at disposal, an increase in mesh size and thus decrease in resolution was necessary for the investigations regarding PDMS. An easy solution to this problem would be to simulate on computers with a higher amount of RAM.

# Bibliography

[1] M. Antfolk, S. H. Kim, S. Koizumi, T. Fujii, and T. Laurell, *Label-free single-cell separation and imaging of cancer cells using an integrated microfluidic system.* Scientific Reports **7**, 46507 (2017).

[2] I. Gralinski, S. Raymond, T. Alan, and A. Neild, *Continuous flow ultrasonic particle trapping in a glass capillary.* Journal of Applied Physics **115**(5), 054505 (2014).

[3] B. Hammarstrom, T. Laurell, and J. Nilsson, *Seed particle-enabled acoustic trapping of bacteria and nanoparticles in continuous flow systems.* Lab Chip **12**, 4296–4304 (2012).

[4] P. Mishra, M. Hill, and P. Glynne-Jones, *Deformation of red blood cells using acoustic radiation forces.* Biomicrofluidics **8**(3), 034109 (2014).

[5] J. Lei, P. Glynne-Jones, and M. Hill, *Acoustic streaming in the transducer plane in ultrasonic particle manipulation devices.* Lab Chip **13**, 2133–2143 (2013).

[6] M. W. H. Ley and H. Bruus, *Three-dimensional numerical modeling of acoustic trapping in glass capillaries.* ArXiv e-prints. https://arxiv.org/pdf/1704.04300.pdf (2017).

[7] H. Bruus, *Acoustic streaming.* DTU Lecture Notes. www.staff.dtu.dk/bruus (2016).

[8] H. Bruus, *An introduction to the theory of acoustic waves in elastic solids.* DTU Lecture Notes. www.staff.dtu.dk/bruus (2016).

[9] *Comsol multiphysics 5.2.* www.comsol.com (2005).

[10] H. Bruus, *Implementation of first- and second-order acoustic perturbation theory in comsol.* DTU Lecture Notes. www.staff.dtu.dk/bruus (2016).

[11] H. Bruus, *Fluid solid coupling in comsol.* DTU Lecture Notes. www.staff.dtu.dk/bruus (2017).

[12] J. Tsou, J. Liu, A. Barakat, and M. Insana, *Role of ultrasonic shear rate estimation errors in assessing inflammatory response and vascular risk.* Ultrasound in Medicine and Biology **34**(6), 963–972 (2008).

[13] P. B. Muller, R. Barnkob, M. J. H. Jensen, and H. Bruus, *A numerical study of microparticle acoustophoresis driven by acoustic radiation forces and streaming-induced drag forces.* Lab Chip **12**, 4617–4627 (2012).

[14] F. Jacobsen and P. Juhl, *Radiation of sound.* DTU Lecture Notes. http://web-files.ait.dtu.dk/fjac/p_home_page/notes/Radiation.pdf (2011).

[15] J. Renninger, *Understanding damping techniques for noise and vibration control.* E-A-R Speciality Composites, documentation. https://www.rathbun.com/c-26-e-a-r.aspx .